RECRUITMENT AND POLARIZATION OF TUMOR ASSOCIATED MACROPHAGES

by
Haonan Xu

A thesis submitted to Johns Hopkins University in conformity with the requirements for

the degree of Master of Science in Engineering

Baltimore, Maryland
May 2020

ABSTRACT

Macrophages are highly plastic innate immune cells that can be polarized into a range of phenotypes. They have important roles in physiological homeostasis and innate immunity. A subset of anti-inflammatory macrophages has been found to infiltrate the tumor microenvironment, promote tumor immune evasion, initiation, growth, and metastasis. To elucidate the recruitment and polarization of these tumor associated macrophages, an *in vivo* mouse model of immune infiltration, *in vitro* models of recruitment, and *ex vivo* bone marrow derived macrophage (BMDM) studies have been carried out.

Using a syngeneic orthotopic model of mouse pancreatic cancer, it was found that macrophages are preferentially enriched at both primary site and distal organs during tumor development. $CD4^+$ and $CD8^+$ T lymphocyte but not $CD45R^+$ B lymphocyte were also enriched at the primary site. It was further speculated that majority of these macrophages were recruited from circulating monocytes based on their proximity to blood vessels.

Cancer cell paracrine effects on immune cell motility were then evaluated. MDA-MB-231 did not have chemoattraction on human monocyte cell line U937, however, these cancer cells reduced U937 motility. The effects of cancer conditioned media on BMDM motility were then evaluated. Motility data were fitted to the Anisotropic Persistent Random Walk model. Hierarchical clustering showed the cytokine induced M2 (but not M1) BMDM had significantly higher motility and lower heterogenicity. The cancer cell conditioned media treated BMDMs had consistent motility profiles with that of naïve M0 group.

Lastly, cancer cell conditioned media can modulate macrophage mRNA and morphology. Conditioned media from cancer cells seeded at high density are more potent at modulating

macrophage mRNA expression. BMDMs treated with M1/2 polarizing cytokines and KPC conditioned media displayed distinct morphology distributions when compared with M0.

ACKNOWLEDGEMENTS

I would like to thank Dr. Michael Harris, who recruited me for my role here at the Wirtz Lab, showed me ropes to immunology, and more importantly, reassured me why we do what we do. I greatly appreciate his mentorship over both scientific matters and my personal growth as a scientist. I am glad to have had the opportunity of working with him, and even more so in knowing that the scientific community has him.

I would also like to thank Dr. Pei-Hsun Wu for his supervision and guidance. One of the many lessons that I will take beyond my degree here is the engineer's role in comprehending the complex, the convoluted, and the costly. I also take comfort in knowing there is no MATLAB error that Pei-Hsun cannot debug.

Thank you to Professor Denis Wirtz, who has supported and financed my research endeavors as a master's student. My time here has been extremely formative, and I greatly appreciate his inputs, stories, and tweets that inspired me to be the person I am.

Thank you to the members of the Wirtz lab, especially Michelle, Gabby, Bart. Research is not easy, but working alongside you sure made it less difficult. I also want to give a special acknowledgment to Michelle and Bart, who provided critical assistance on carrying out the *in vivo* studies.

Last but not least, I would like to thank the tireless backing of my family and friends. I would not have been where I am today without you, and I am grateful to have you on this journey.

TABLE OF CONTENTS

LIST OF FIGURES

LIST OF TABLES

Chapter 1 – **Introduction**

1.1 Overview of Immune System

We live in a world dominated by microorganisms. All living beings must evolve ways of defending themselves from potentially pathogenic foreign bodies. Not only is the immune system not unique to humans, the first primitive immune system likely existed millions of years before modern humans emerged.

Humans and other mammals have evolved a complex immune system that communicates within a network or small molecules, proteins, cells, vasculatures, and organs[1,2]. This tightly regulated network is responsible for defense against pathogens, communication with microbiota, and maintenance of tissue homeostasis[3–5]. The immune system can be divided into two major branches, the innate immune system and the adaptive immune system.

The innate immune system is composed of a noncellular component made up of plasma proteins, and a cellular component consisting of phagocytic cells and innate lymphoid cells[2,6]. The plasma proteins known as the complement system can rapidly trigger proteolytic cascades to cripple invading microbes while also modulating innate and adaptive immune cell activations[6]. Phagocytes in the innate immune system recognize Pathogen-Associated Molecular Patterns (PAMPs) through Toll-Like Receptors (TLR)[7,8]. Through complex interactions with scavenger receptors, these cells can engulf pathogens and debris from dead cells. The phagocytosed antigens are further processed and loaded on Major Histocompatibility Complexes class II (MHC II) for

presentation to T cells[7,9]. While macrophages participate in bridging the innate and adaptive immune systems, dendritic cells (DCs) are the most efficient antigen presenting cells[1,9].

Adaptive immune system is slower acting in comparison, it consists highly specific B- and T-lymphocytes. Adaptive immune system assembles antigen specific recognition structures by shuffling somatic gene elements, and subsequently selecting for cells with optimal antigen binding capacities during lymphocyte maturations[2,10]. These processes, termed V(D)J recombination and clonal selection respectively, are capable of generating unique antigen binding motifs on the scale of ~10^{11} while simultaneously limiting autoreactive lymphocytes[1,11–13].

Immune system also maintains memories. It has long been shown that B- and T-lymphocytes can give raise to memory cells that are capable of self-renewing and sustaining antigen specific immunity up to the lifetime[14–16]. This immunological memory provides efficient defense against reoccurring infections and is critical for prophylactic vaccine developments. In the recent times, it was further demonstrated innate immune cells such as monocytes, macrophages, and natural killer cells (NKs) are also capable of maintaining immunological memories termed "trained immunity"[17,18]. Although circulating monocytes have short lifespan (~24 hours), their trained immunity can last for months through epigenetic modification of bone marrow progenitors[17,19]. Upon re-challenge, these primed monocytes exhibits stronger immune response[17].

1.2 Overview of Macrophages

1.2.1 Macrophage Receptors and Functions

Macrophages are professional phagocytes and antigen presenting cells. Along with other phagocytic cells such as monocytes, DCs, neutrophils, and mast cells, macrophages express a multitude of scavenger and pattern recognition receptors (PPRs) (Table 1)[7]. Through complex interactions, these receptors can recognize damage associated molecular patterns (DAMPs) or PAMPs from cellular debris and invading microbes. Macrophages therefore maintain a critical role on initiating innate immunity and maintaining tissue homeostasis.

Table 1. Selective Macrophage Surface Receptors

Receptor	Class	Target	Function	Ref
CD36	Scavenger	Oxidized LDL, diacyl fatty acids	Phagocytosis of apoptotic cells, recognition of microbial cell walls	[20]
CD163	Scavenger	Hemoglobin-haptoglobin complex	Phagocytosis of apoptotic cells	[20]
MACRO	Scavenger	CpG-ODNs	Bacterial recognition, positive regulation of NO and IL-12 production	[20,21]
CD14	GPI-anchored	LPS, LTA, PGN, Phospholipids	Recognition of apoptotic cells, possible coreceptor to TLR2 and TLR4	[20]
MRC1 (CD206)	C-type 1 Lectin	Mannose, fucose, N-acetylglucosamine	Endogenous glycoprotein clearance, antigen presentation, pathogen recognition, potentially involved in leukocyte migration	[20,22]
Itgam (CD11b)	Integrin	C3bi, ICAM-1, and others	Regulates pro-inflammatory macrophage activation	[20,23,24]

FcγRI	Ig Superfamily	IgG1 (high affinity), IgG3 (high affinity), IgG4	FcR mediated opsonic phagocytosis	1,20,25
Siglec-1 (CD169)	Ig Superfamily	Sialic acid	May be involved in host cell recognition	20
Siglec-10	Ig Superfamily	CD24	Phagocytic checkpoint, blockade of CD24 to Siglec10 interaction leads to phagocytosis of $CD24^{+}$ cancer cells	26
SIRPα	Ig Superfamily	CD47	Phagocytic checkpoint, expression of CD47 on erythrocytes prevents phagocytosis	20,27
CR3	Complement Receptor	C3bi	Heterodimer of CD11b and CD18, complement mediated opsonic phagocytosis	20,28
C5aR1	Complement Receptor	C5a	Binds C5a, complement mediated macrophage activation	23
TLR1	TLR	Bacterial lipoprotein	PAMP recognition	8,23
TLR2	TLR	Lipoproteins, LTA, PGN, viral proteins, fungal mannans	PAMP recognition	8,23
TLR4	TLR	LPS, fungal mannans, parasite glycoinositol-phospholipids	PAMP recognition	8,23
TLR5	TLR	Flagellin	PAMP recognition	8,23
TLR6	TLR	Bacterial lipoproteins, fungal zymosan, β-glucan	PAMP recognition	8,23
CCR2	Chemokine Receptor	CCL2 (MCP-1)	Recruitment of monocytes, modulation of chemotaxis	29
CXCR4	Chemokine Receptor	SDF1α	Recruitment of monocytes	29

CSF1R	Cytokine Receptor	CSF-1	Regulation of macrophage proliferation and survival	29

1.2.2 Development of Macrophages

Macrophages are found in a wide range of tissue types with diverse functions[30,31]. Microglial cells maintaining homeostasis of the brain, splenic red pulp macrophages recycling red blood cells, and peritoneal cavity macrophage facilitating IgA productions are all examples of tissue resident macrophage funcitons[30,31]. Unlike the circulatory pool of monocytes that differentiated from bone marrow progenitors, most of tissue resident macrophages are of the embryonic origin (Figure 1) [30]. These cells are capable of self-renewal and proliferation which is likely a result of shared transcription factors PU.1, C/EBP, and MAF[30]. Osteoclasts are essential for bone remodeling, while it is not well understood if these cells originated from embryonic tissue, it was shown that monocytes can differentiate into osteoclast[31]. Moreover, the circulatory monocytes can also serve as an emergency pool; in cases of severe inflammatory injury, monocytes can extravasate out of circulation to replenish macrophage populations[32].

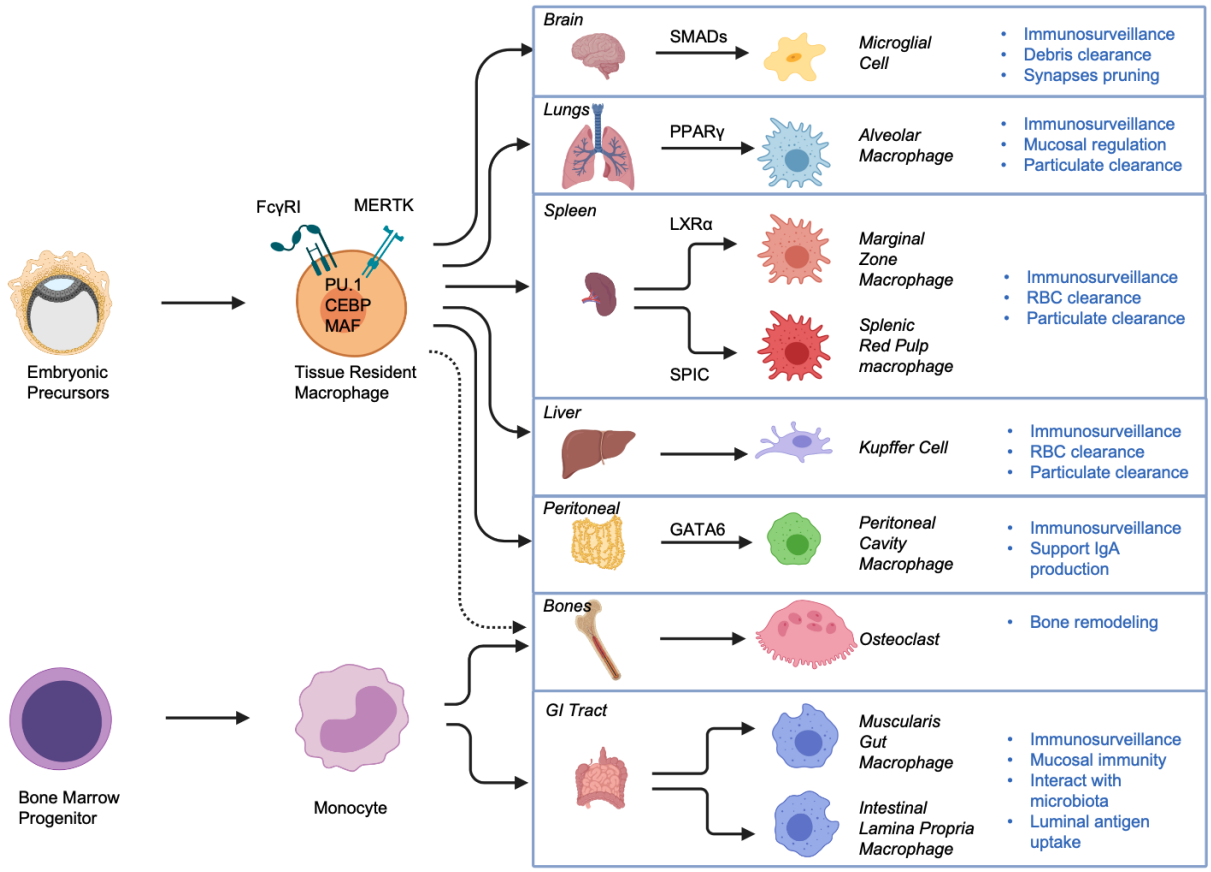

Figure 1. Macrophage Development and Function

Macrophages are derived from two lineages, embryonic and monocytic. Most of tissue resident macrophages are generated from embryonic precursors, whereas monocytes are circulatory and serve as a progenitor pool in the event of severe inflammatory injuries. During development, cells from embryonic origin enter various tissue microenvironments, adapt and proliferate within the local niches, and self-renew continuously throughout the lifespan. Monocyte progenitors are of hematopoietic stem cell linage, they reside in bone marrow with longevity.

1.2.3 Macrophage Polarization

Macrophages also have remarkable plasticity. Historic understanding defines two polar opposite states, classically activated M1 or pro-inflammatory phenotype, and alternatively activated M2 or anti-inflammatory phenotype. However, vast evidences suggested there are

actually multiple phenotypically stable and distinguishable states of polarized macrophages, and their transcriptomic signatures range across a spectrum[33–35]. For instance, within the anti-inflammatory branch, M2a is polarized by T_H2 cytokines interleukin-4 (IL-4) and interleukin-13 (IL-13), M2c is stimulated by interleukin-10 (IL-10), and M2f by engulfing apoptotic cells[22,36]. Functional outcomes of these macrophages are different, M2a promotes angiogenesis by secreting platelet-derived growth factor BB (PDGF-BB), M2c promotes matrix remodeling through matrix metalloproteinase (MMP) expressions, and M2f inhibits inflammation though autocrine/paracrine signaling[36–38]. Surprisingly, the physiological roles assigned to classical M1/M2 paradigm can overlap too. While M2 phenotype is traditionally associated with tissue homeostasis, Graney and colleagues recently demonstrated that classical M1 macrophages also promote vascularization by inducing pro-angiogenesis genes in endothelial cells[36]. To that extent, we defined M1 and M2-like macrophage phenotypes based on the activation stimuli, markers, and function (Figure 2)[22,36,38–43].

It is important to note that macrophages and myeloid derived dendritic cells share numerous transcriptional regulations, surface marker expressions, and functional features[7,44]. It is not readily possible to distinguish these cells of the mononuclear phagocyte system, therefore the newly proposed nomenclature calls for classification by ontogeny[45]. For the scope of this thesis, human monocytic cell line U937 derived macrophages and murine primary bone marrow derived macrophages (BMDMs) were investigated.

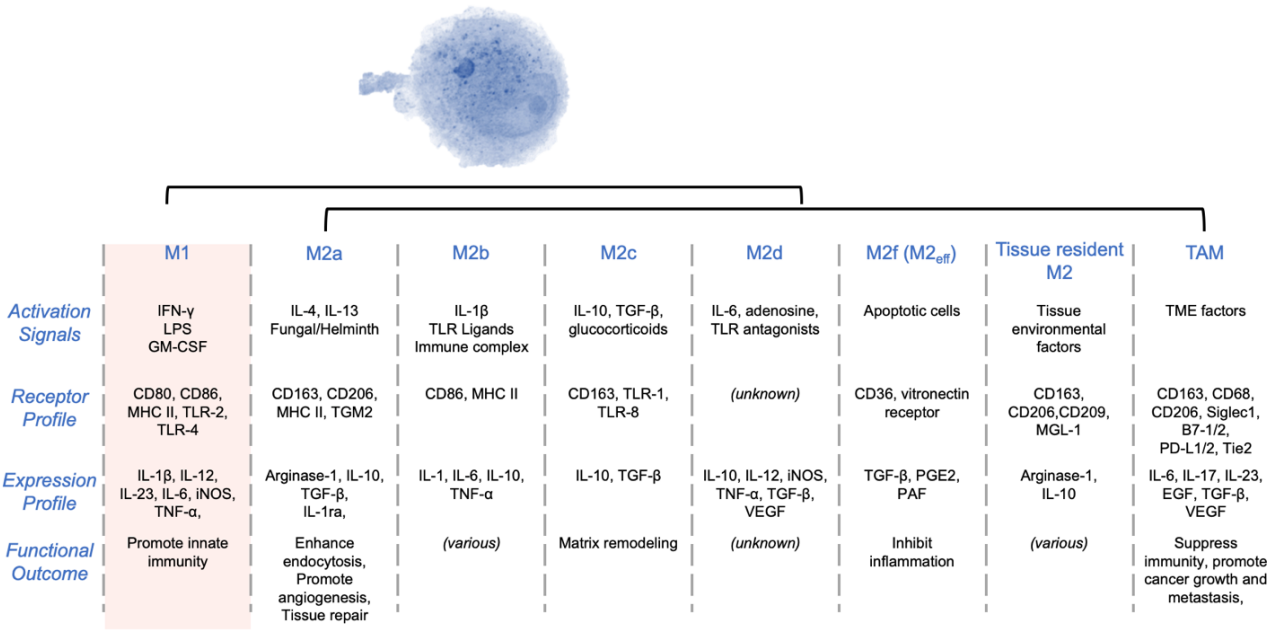

Figure 2. Classification of Macrophage Phenotypes

Macrophages are classified into a pro-inflammatory M1 phenotype and a range of M2-like phenotypes. Historically defined binary paradigm of M1 M2 polarization does not accurately depict the diverse macrophage phenotypes. Here, M2a, M2b, M2c, and M2d have well understood activation signals, although physiological functions may overlap. M2f (or $M2_{eff}$) macrophages arise from engulfment of apoptotic cells, a process known as efferocytosis. Upon activation, M2f macrophages downregulate pro-inflammatory cytokines such as IL-1β, IL-8 and GM-CSF through autocrine and paracrine signaling. Tissue resident macrophages maintain diverse phenotypes and functions (Figure 1). TAMs are considered M2-like here for its compacity to suppress antitumor immunity and promote intertumoral vascularization. There are also arguments for TAM not being a macrophage subset since it does not confer a steady state phenotype. The image shown was the maximum intensity projection of a U937 derived macrophage under 3-D quantitative phase imaging, a result of collaboration with Dr. Ishan Barman.

1.3 Tumor Associated Macrophages

Macrophages are among the most abundant cells types in tumor microenvironments (TMEs)[40]. Despite their prominent role in innate immunity, tumor infiltrating macrophages are not usually tumoricidal[31,41]. In fact, tumor associated macrophages (TAMs) have been shown to promote cancer initiation, growth, and metastasis[31,41]. Mechanistically, TAMs can generate

chronic inflammation that aids the initiation of malignancies, suppress T lymphocyte activities to prevent immunogenic cancer cell killing, promote angiogenesis to maintain tumor growth, and degrade ECM network to improve cancer cell dissemination (Figure 3)[31,41,46]. Although TAMs may share some gene expression features with M1 macrophages, they are widely recognized as anti-inflammatory (M2-like)[33].

Given their abundance in TMEs and trainable plasticity, TAMs has been regarded as a promising therapeutic target. Current clinical studies includes both small molecules and antibody drugs aimed at obliterating TAMs, preventing monocyte recruitments, re-educating TAMs towards pro-inflammatory phenotype, or blocking phagocytosis checkpoints[29]. Notably, a PI3Kγ signaling pathway targeted drug (Ibrutinib) intended to reprogram TAMs and reduce myeloid infiltration is under phase III clinical trial for metastatic pancreatic adenocarcinoma (PDAC) treatment (combination with gemcitabine and nab-paclitaxel, NCT02436668)[29]. Elucidation of macrophage mediated tumor immune evasion therefore has significant merits in immuno-oncology.

The pathological functions of TAMs are growing clear, but their polarization from naïve phenotypes remains to be fully characterized. In recent years, there are some promising results suggesting chemokine signaling, metabolic regulation, and checkpoint escape are some immune evasion mechanism[26,47–50]. For instance, Myosin II in tumor invasive fronts cross-talk with IL-1α/NF-κB to release TAM-polarizing cytokines and chemokines[50]. It was also shown cancer cell secreted retinoic acid can induce monocyte differentiations into macrophages preferentially over DCs, and its blockage results in enhanced anti-tumor T cell immunity[49]. Our results suggest that the cancer cell paracrine signaling may also modulates the migration and recruitment of macrophages.

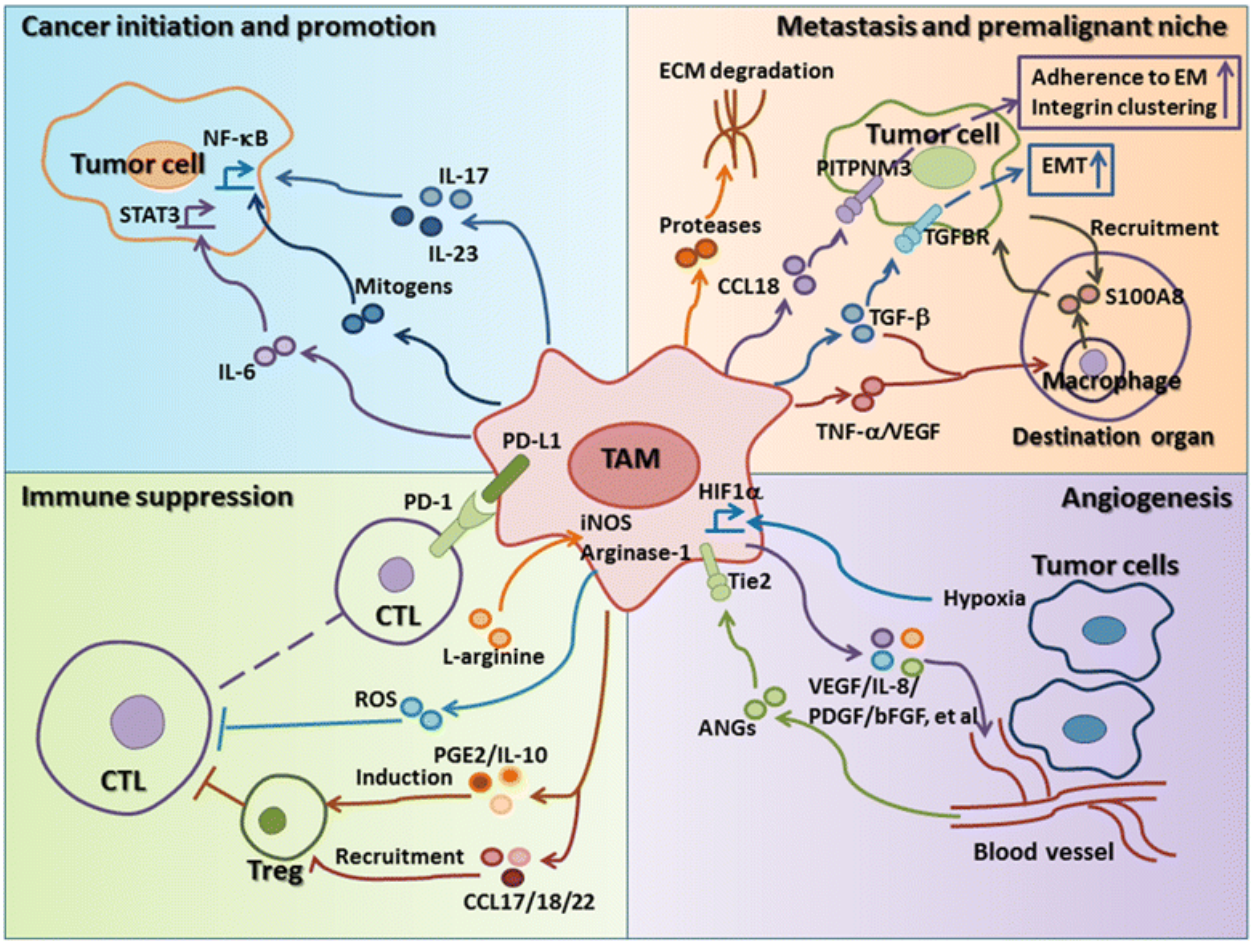

Figure 3. Roles of Tumor Associated Macrophages

Tumor associated macrophages holds diverse roles in tumorigenesis. The TAMs secreted cytokines and chemokines can promote tumor initiation and metastasis. Widely accepted as M2-like, TAMs can also suppress anti-cancer T cell immunity and promote tumor vascularization. For immune suppression, both direct suppression such as checkpoint mediated escape and indirect suppression involving regulatory T cell have been shown. Furthermore, tumor size is depended on the available nutrient and oxygen transport to the core, under poor vasculature network, hypoxia can switch on the production of pro-angiogenic factors in TAMs whereby further tumor growth is sustained. This figure was reprinted from the work of Yang & Zhang under the Creative Commons CC BY license[41].

1.4 Tumor – Immune Interaction

1.4.1 Cancer Immunoediting

An essential prerequisite for both innate and adaptive immunity is the ability to discriminate self from nonself[2]. During anti-bacterial or anti-fungal immunity, immune systems can recognize conserved endotoxins, sugars, or membrane structures (Table 1) as foreign. However, anticancer immunity can be more intricate due to the vastly diverse cancerous cell types with varying degree of tumorigenic potential; in addition, the complex TME also dictates cancer cell fates and degree of immune cell infiltrations[51,52]. Besides clonal evolution (a process where cancer cells randomly accumulate mutations and become more or less advantageous at survival and proliferation), "cancer immunoediting" also contributes to the tumor heterogenicity and evolution of cancer cells[52,53]. Cancer immunoediting refers to the idea that immune surveillance acts as an evolutionary selection pressure for cancer cells, the resulting "edited" tumor should only be composed of immunologically undetected cancer cells[54]. Effectively, cancer immunoediting can lead to three outcomes: 1) complete cancer rejection due to immunogenic cancer cell death, 2) an equilibrium between cancer cells and immune system which leads to long term cancer dormancy, and 3) cancer immune evasion, which leads to local or systematic outbreak of cancer growth[55,56]. Although cancer dormancy and immuno-equilibrium do not manifest detectable symptoms, this equilibrium is evidenced by multiple transmission of cancers from an apparently heathy donors[57,58]. Importantly, cancer clonal evolution and immunosurveillance may also have defining power over the capacity and location for secondary metastasis. Metastasis has been suggested to have a "seed and soil" relationship with secondary lesion sites[59]. In other words, organ-tropical metastatic cancer cells must adapt to new tissue environments, and new tissue

immune environments must be permissive for cancerous growth[59–61]. In a particular mouse study, bone marrow derived VEGFR1$^+$ hematopoietic progenitors arrive at pre-metastatic site long before primary tumor cells, and are important for tumor metastasis[62,63]. Neutrophils have been implicated in initiating metastasis as well[64,65].

1.4.2 Antitumor Immunity

Tumor immunity is an arms race between pro-tumor immune modulators and anti-tumor immune modulators. Besides TAMs, regulatory T cells (T_{reg}), Th2, N2, DC2, myeloid-derived suppressor cells (MDSCs), and B cells have all been shown to be tumor promoting, whereas cytotoxic T cells, Th1, N1, DC1, NK, and M1 macrophages are tumor rejecting[54,66]. Immunological tumor rejections can be achieved through a wide range of mechanisms, including the use of certain chemotherapeutic agents that promote cancer antigen uptake and presentation[67]. Here we emphasize macrophage mediated T cell activities (Figure 4). Although DCs are more efficient APCs, macrophages can in theory stimulate T cell mediated anti-tumor response by fulfilling the three T-cell activation signals. For signal 1, engulfed antigen must be digested, processed, and loaded on MHCII for presentation to TCR. Then costimulatory molecules and activating cytokines constitute signal 2 and signal 3 respectively[68]. Upon activation, T cells can then trigger a cascade of antitumor responses including direct binding and killing specific antigen expressing cancer cells[68].

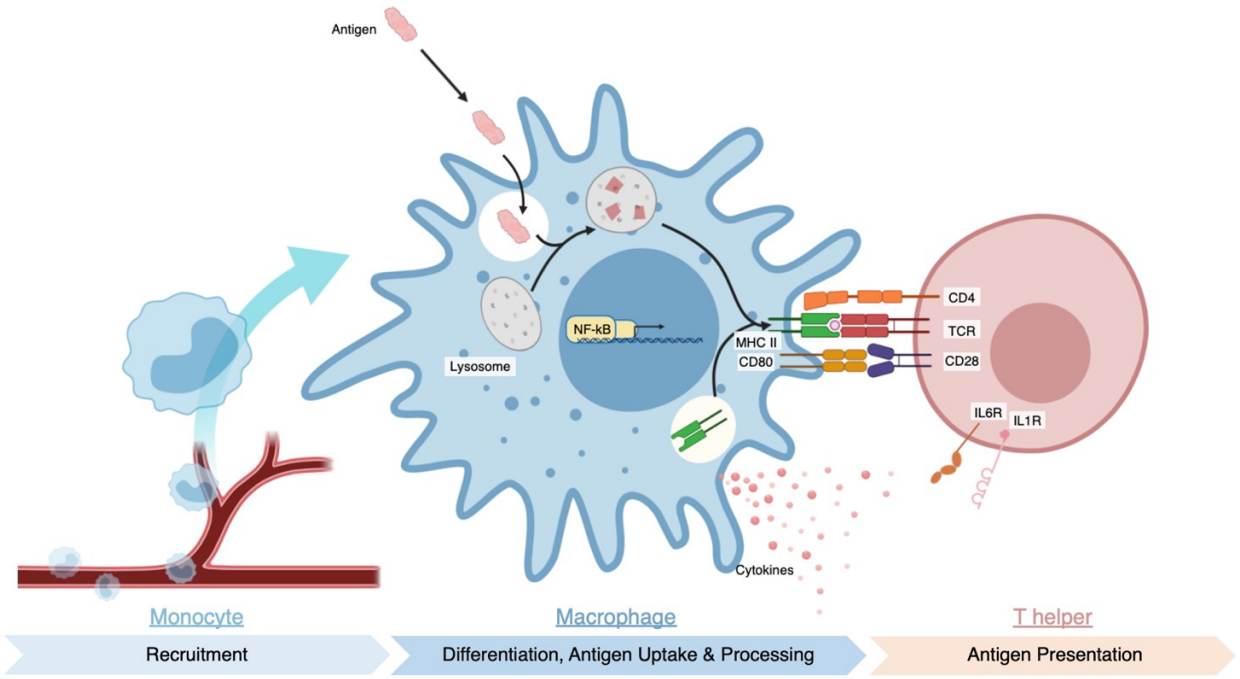

Figure 4. Macrophage Mediated Immunosurveillance

Macrophage (dendritic cell shares similar process) mediated immunosurveillance can be classified into three stages, monocyte recruitment, differentiation & antigen uptake, and antigen presentation. At monocyte recruitment stage, DAMPs or PAMPs modify local endothelial cells, which in turn increase monocyte adhesion and promote extravasation from vasculature. At the site of inflammation, monocytes differentiate into macrophages and migrate under a chemotactic gradient. Upon encountering antigens, the microphage engulfs the foreign bodies by engaging various scavenger receptors and PRRs. The antigen is then broken down in lysosome then loaded onto MHC II. Peptide loaded MHCII serves as 1st of 3 signals required for T cell activation. Co-stimulatory receptors like CD80 and T cell stimulatory cytokines such as IL-6 or IL-1 β are 2nd and 3rd signal respectively. Upon successful antigen presentation and T cell activation, T cell mediated adaptive immunity can be initiated. Tumor immune evasion can be achieved by interferences at any of the stages.

Chapter 2 – **KPC PDAC Immune Landscape**

2.1 Introduction

2.1.1 Pancreatic Ductal Adenocarcinoma

Pancreatic Cancer remains a lethal and prevent disease. Over 450,000 new cases were reported globally in 2018, the overall 5 year survival rate is about 10%, and for metastasized cases, the survival rate is less than 5% [69,70]. Among all the subtypes, PDAC is the most common type of pancreatic cancer, accounts for more than 80% of all cases[70]. This considerable mortality rate is partly caused by asymptomatic disease progression, which leads to late diagonosis[70]. One report suggested the carcinogenesis for pancreatic cancer is remarkably slow, taking at least 10 years after the first genomic mutation to give raise to the first non-metastatic cancer cell, which would then take 5 more years to gain metastatic potentials[71]. In addition, the pancreatic cancer TME is pathologically complex. Dense fibrotic ECM protects cancer cells from chemotherapy, and TAMs release pyrimidines to inhibit gemcitabine efficacy[72,73].

2.1.2 Origins and Functions of TAMs

It was recently demonstrated that macrophages of both monocytic origin and embryonic origin contribute to PDAC TME remodeling[74]. Zhu and colleagues showed that monocyte derived TAMs have higher antigen uptake and presentation capacity, whereas embryonic TAMs had enhanced matrix remodeling transcriptional signatures[74]. Under physiological conditions, tissue resident macrophages can proliferate *in situ* in response to mild traumas, whereas severe

inflammatory injuries call for monocyte extravasation and differentiation into macropahges[32]. It appears these cells of distinct linkages also conspire during tumorigenesis. Along with prior evidences of monocytic macrophages' roles in cytotoxic T lymphocyte exclusion and poor patient survival, these findings depicts a complex immune landscape during tumor progression[75,76].

Aimed at understanding the temporal immune landscape during tumorigenesis, we carried out orthotopic syngeneic PDAC study using the same *Trp53*^{R172H} *Kras*^{G12D} spontaneous cancerous KPC cells[74,77].

2.2 Materials & Methods

2.2.1 Regulatory Compliance

Orthotopic PDAC model was carried out using female C57BL/6 mice (Jackson Laboratory) at 9 weeks of age . The study was reviewed and approved by institute Animal Care and Use Committee under protocol number M018A61.

2.2.2 Pre-Surgery Preparations

Two days prior to the orthotopic injection, subjects underwent hair removal by Nair. The day before surgery, enrofloxacin was given at 5 mg/kg body weight subcutaneously (per veterinarian's prescription) to reduce the risk of infection.

2.2.3 Sample Preparation

Matrigel (Corning) scaffold was allowed to thaw on ice at 4 °C overnight. On the day of surgery, cancer cells were dissociated from culture and resuspended in PBS at 1000 cells/μL. 10,000 cells were then mixed with equal volume of Matrigel, constituting 20 μL total injection volume. Surgical control group received equal volume of PBS/Matrigel without cancer cells. The cells were then kept on ice during the transport to animal holding facility.

2.2.4 Laparotomy and Injection

Animals were incubated in isoflurane induction chamber until immobile, and general anesthesia was achieved using an isoflurane vaporizer and nose cone. Buprenorphine SR (0.5 mg/kg) and the second dose of enrofloxacin were given subcutaneously.

2-cm incision was made on the left subcostal region along transverse plane first through dermis then peritoneum layer. Spleen was exposed by compressing against the opening. By carefully pulling the spleen, pancreas was exposed and the injection could be made. The test subjects received 10,000 KPC cells with Matrigel scaffold, and the control subjects received only scaffold. Spleen and pancreas were then placed back into cavity. The peritoneum and dermis were then sequentially sutured. The animals were then placed on heating pad until consciousness was regained. The post operation recovery was monitored at following day, and sutures were replaced as needed.

2.2.5 Endpoint Processes

At each timepoint, subjects were euthanized. Primary tumor as well as liver, spleen, kidney, and inflated lungs were excised, placed in tissue cassettes, and fixed in formalin (VWR) solution overnight before replacing in PBS buffer. The lungs were inflated by injecting 1.5% agarose through trachea using a 18-G blunt fill needle (BD) . The agarose was melted in a microwave and maintained above 65 °C using a heat block. Needles and syringes were also prewarmed using the heat block to reduce blockage. The formalin fixed samples were then delivered to Oncology Tissue Services core for paraffin embedding, slicing, histology stains, and scanning.

2.2.6 Primary BMDM Extraction

Mouse bone marrow derived macrophages (BMDMs) were harvested from C57BL/6J mice based on an established protocol[78]. In brief, mice were incapacitated with isoflurane (VET One, Fluriso) and euthanized in compliance with institute ACUC regulations. Hindlimb femurs and tibias were excised and sterilized with 70% ethanol. Proximal ends of the bones were severed, and a 26-G needle (BD) was inserted in distal ends. Marrow was flushed out with PBS (Corning) and dissociated by pipetting. The cells were then pelleted, washed, and seeded in T-75 flasks.

Primary mouse BMDMs were grown in DMEM (Corning 10-013-CV formulation) with 10% HI-FBS and 100 U/mL Murine M-CSF (Prospec Protein, Cat # cyt-439). Fresh media was supplemented every two days, and the cell culture was maintained and expanded in culture for at least 7 days before assays. The protocol was validated to generate $CD11b^+$ $F4/80^+$ macrophages by flow cytometry (Figure S3).

2.3 Results

To characterize the temporal immune cell landscape during tumorigenesis, we orthotopically implanted the KPC GFP$^+$ Luc$^+$ cancer cells to C57BL/6 mice. Reporter tagged cells were used for the ease of tumor burden measurements. Prior experience working with orthotopic KPC models indicated an aggressive cancer phenotype and consequently short life span (4 weeks). Therefore, the experiment timeline was set for 3 weeks to profile B lymphocyte, T lymphocyte, and macrophage landscape within the primary tumor (Figure 5A). IHC staining showed a drastic increase of F4/80$^+$ macrophage populations (Figure 5B), from almost nonexistent in WT control and PBS surgical control groups, to approximately 30% of total quantified pixel signals (Figure 5C, 5D). This recruitment was also observed in kidney, liver, and spleen (Figure S1B).

Temporal depended CD4$^+$ and CD8$^+$ T cell enrichment was also observed, although no CD4$^+$ and CD8$^+$ T cells were detected in healthy WT control (Figure 5E, Figure S1A). Any tissue-resident memory T cells (TRMs) that are important for immunosurveillance and homeostatic maintenance are likely below the detection limit[79]. Interestingly, CD45R$^+$ B lymphocytes did not confer to any discernable pattern. While it is possible that B lymphocytes were not enriched during tumorigenesis, CD45R antibody also has higher background noise and less cell type specificities when compared to the other IHC antibodies used (Figure S1A).

Lastly, areas of CD11b$^+$ macrophage infiltration coincides with areas of vasculatures at 1 week post implantation. This result suggests that observed macrophage populations originated from the monocytic pool. Although it is not possible to speculate the degree of monocyte infiltration as tissue resident macrophages may also undergo clonal expansion[74].

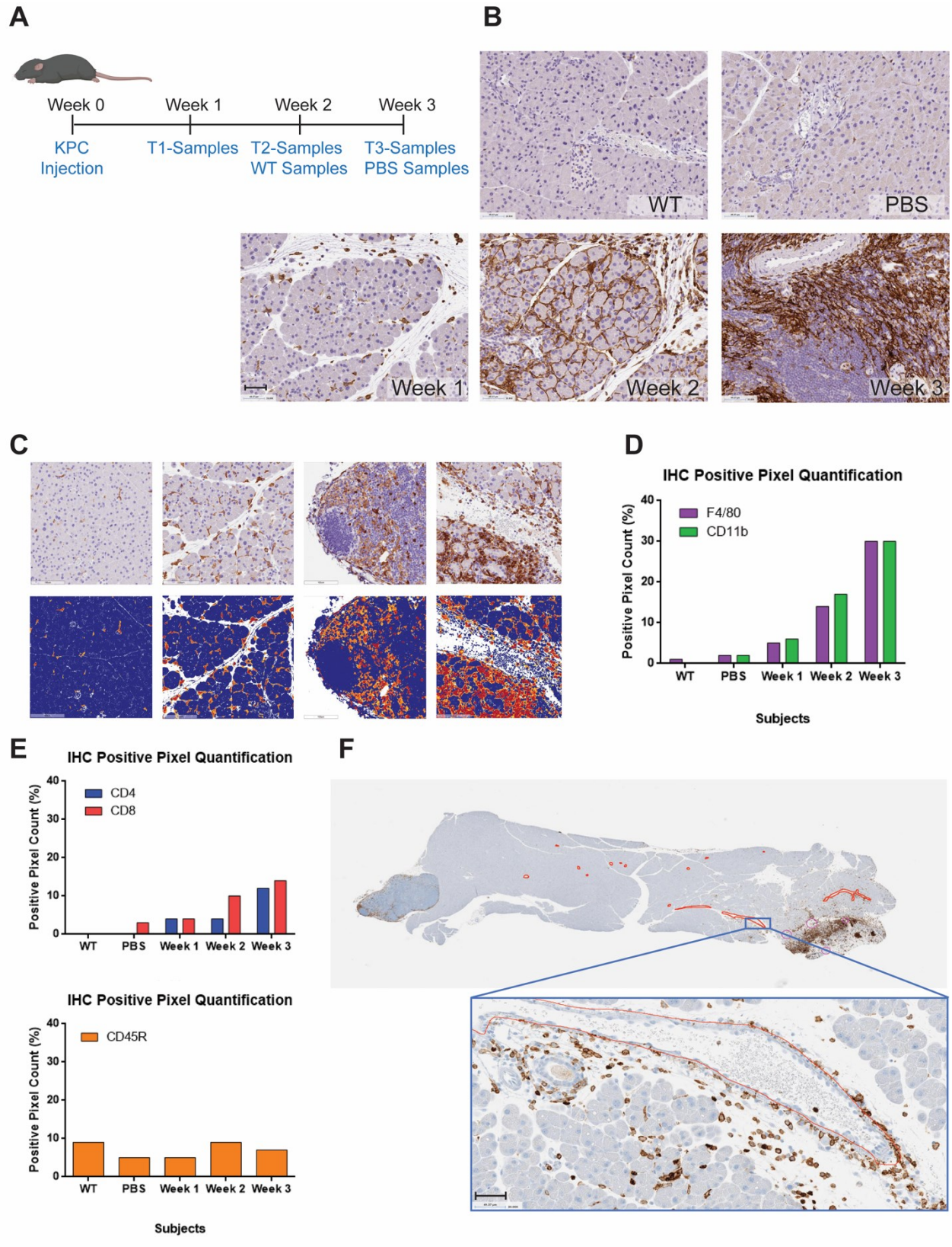
A
Week 0
Week 1
Week 2
Week 3
KPC Injection
T1-Samples
T2-Samples WT Samples
T3-Samples PBS Samples
B
WT
PBS
Week 1
Week 2
Week 3
C
D
IHC Positive Pixel Quantification
F4/80
CD11b
Positive Pixel Count (%)
WT
PBS
Week 1
Week 2
Week 3
Subjects
E
IHC Positive Pixel Quantification
CD4
CD8
IHC Positive Pixel Quantification
CD45R
F

Figure 5. Temporal Immune Landscape during KPC Tumorigenesis

(A) Overview of the experimental schedule for evaluating temporal immune landscape.
(B) IHC stain of F4/80$^+$ macrophages within pancreas, the primary cancer cell injection site
(C) Representative images of IHC signal quantification using ImageScope. Positive signals are shown on a gradient from yellow to red corresponding to signal intensity. Negative signals are shown in blue, and backgrounds are uncolored.
(D) Quantifications of F4/80$^+$ and CD11b$^+$ macrophages in pancreas. CD11b$^+$ IHC for WT was not available.
(E) Quantifications of CD4$^+$, CD8$^+$ T cells, and CD45R$^+$B cells.
(F) High magnification view of CD11b$^+$ macrophages. Blood vessels are annotated in red, RBCs without endothelial structures are annotated in magenta.

n = 1 subject, additional biological repeats are available but not processed. Scale bar, 50 μm.

2.4 Discussion

In this study, WT control shows a healthy steady state immune cell abundance within the pancreas, whereas PBS surgical control accounts for the inflected trauma, possible infection, and potential Matrigel scaffold immune reactivities. A significant enrichment of macrophage were seen in primary tumor site (indicated by F4/80$^+$ and CD11b$^+$ IHCs) and distal organs (indicated by F4/80$^+$ IHC). This observation indicates KPC cells can modulate macrophage on a systematic level. It is possible that macrophages may also facilitate the remodeling of pre-metastatic niches like neutrophils or bone marrow hematopoietic progenitors[62–65].

Furthermore, T cells (indicated by CD4$^+$ and CD8$^+$ IHCs) but not B cells (indicated by CD45R$^+$ IHC) enrichment was observed during tumorigenesis. While T cell infiltration (either CD4$^+$ and CD8$^+$) did not reach the abundance level macrophages did, it is still difficult to speculate if one of these cell types facilitated the recruitment of the others. The difference in abundance between CD4$^+$ and CD8$^+$ lymphocytes is also smaller at week 3 than week 2. It is perceivable that a fraction of the CD4$^+$ T cells are FoxP3$^+$ regulatory T cells, which can suppress cytotoxic T mediated cancer cell killing.

Working with reporter tagged cells may allow easier disease burden tracking, but the reactivity of these probes should also be considered. Specifically, the CTL epitope of luciferase may bind to murine IFN-γ receptors and trigger $CD8^+$ T cell activities[80,81]. To address this concern, the subsequent BMDM *ex vivo* experiments were carried out using unlabeled KPC parental strain.

Chapter 3 – **Macrophage Motility and Recruitment**

3.1 Introduction

3.1.1 Immune Cell Migration

Coordinated migration is essential for immune cell function. During inflammation or pathogen invasion, non-tissue resident immune cells like neutrophils and monocytes need to extravasate from vasculature, and navigate through ECM[82,83]. The migration through blood vessel, known as the leukocyte recruitment cascade is relatively well understood. Local inflammation induces adhesion molecules in endothelial cells, promote leukocyte tethering, rolling, adhesion, crawling, and eventual transmigration[82]. For the second part, migration through ECM can be challenging, some adaption to remodel ECM or squeezing through matrix proteins are needed[83]. Here, we are taking a reductionist approach to examine the BMDM motility using 2D cell migration.

3.1.2 Chemo Gradients

Once leukocytes leave blood vessel, the migration towards the site of inflammation within ECM is usually guided by chemotactic gradients[82]. At steady state, free of stimulations, 2D cell migration patterns are random when the cell maintains little intrinsic directionality (Figure 6A)[84,85]. The intrinsic directionality here is reflected under uniformly imposed signals that affect motility machineries but not directions[84]. If a stimulating signal (either positive or negative) were given symmetrically, motility can either be enhanced or suppressed without affecting the directionality

of the cells, known as chemokinesis (Figure 6A) [84,86]. In contrast, chemotaxis (and chemorepulsion) occurs when an asymmetric soluble factor gradient drives directional migration towards (or away from) the higher concentration (Figure 6A)[84,85,87]. Importantly, the same signaling molecule at different concentrations may drive both chemotactic attraction or repulsion[87].

To understand the chemotactic relationship that leads to monocyte (and other immune cell) requirement to tumors, we performed a proof of concept study by carrying out cell-to-cell chemotaxis assay using MDA-MB-231 breast cancer cells and U937 monocytes.

3.1.3 Random Walk Models

2D cell motility has long been described by cell speed and persistence using Persistent Random Walk (PRW) model[86,88,89]. Under physiological conditions, 3D environment is complicated by ECM topology, molecular composition of ECM, and other features such as ECM crosslinking, matrix stiffness and density[83]. Therefore the cell motility in 3D environment is dependent on specific ECM conditions as well as cell mediated matrix remodeling (i.e. expression of metalloproteinases). Its anisotropic nature does not meet the requirements of PRW. To factor in the differential migration pattern along the primary axis and an orthogonal secondary axis, Anisotropic Persistent Random Walk (APRW) model is better fitted for 3D migration[88,89].

While 2D motility is evaluated for BMDMs, APRW provides better characterization of cell motility biases.

3.2 Material & Method

3.2.1 μ-slide chemotaxis

Cells were seeded on μ-slide chemotaxis chip (ibidi) according to the manufacturer's recommendations. U937 cells were seeded in collagen I (Corning, Rat Tail, High Concentration) at 2 mg/ml. The gel was allowed to set in the central channel at 37 ºC for one hour before liquid media or MDA-MB-231 cells were added to surrounding chambers.

3.2.2 Primary BMDM Polarization

Primary BMDM extraction method is described in section 2.2.6. BMDM were cultured in the presence of M-CSF for 7 days. For M1 polarization, cells were cultured with 20 ng/mL IFN- γ (PeproTech, 315-05) and 100 ng/mL LPS (List Biological Lab, 421) for 24 hours. For M2 polarization, cells were cultured with 20 ng/mL IL-4 (Prospec, cyt-282) for 24 hours. Fresh media were used for M0 macrophages. Polarization protocol is adapted from a literature reference[90].

3.2.3 Generation of KPC Conditioned Media

For high density and low density KPC conditioned media, 2 million and 1 million KPC cells were separately seeded in 10 mL of DMEM complete media in T-75 flasks. On day 2, supernatant was harvested and filtered using a 0.22 μm polyethersulfone syringe filter (Millipore). The conditioned media was stored at -80 ºC. At the time of treatment, conditioned media were added to 3 volumes of fresh media in order to prevent nutrient starvation (Figure 6).

3.3 Results

3.3.1 Monocyte Recruitment

The *in vivo* study demonstrated the possibility of monocyte recruitment to a tumor site. To understand if cancers have chemotactic capacities, we carried out a proof of concept cell-to-cell chemotaxis assay using commercially available microfluidic channels (Figure 6B). When a gradient of cancer cell signaling molecules were created, U937 monocytes had a marginal increase in distance travelled towards MDA-MD-231 (Figure 6D). However, the relatively small cell number (15 cells towards from cancer cell chamber, 23 cells away) does not definitively suggest that a chemotactic relationship exists. When MDA-MD-231 cells were seeded in both chambers next to U937 cells (Figure 6C), the overall distance traveled seems to be smaller than that with only one chamber. Quantification of mean velocity per frame, mean-squared displacement over time, and diffusivity fitted through APRW model (Figure 6E – G) all suggested increased cancer signaling is associated with reduced monocyte motility.

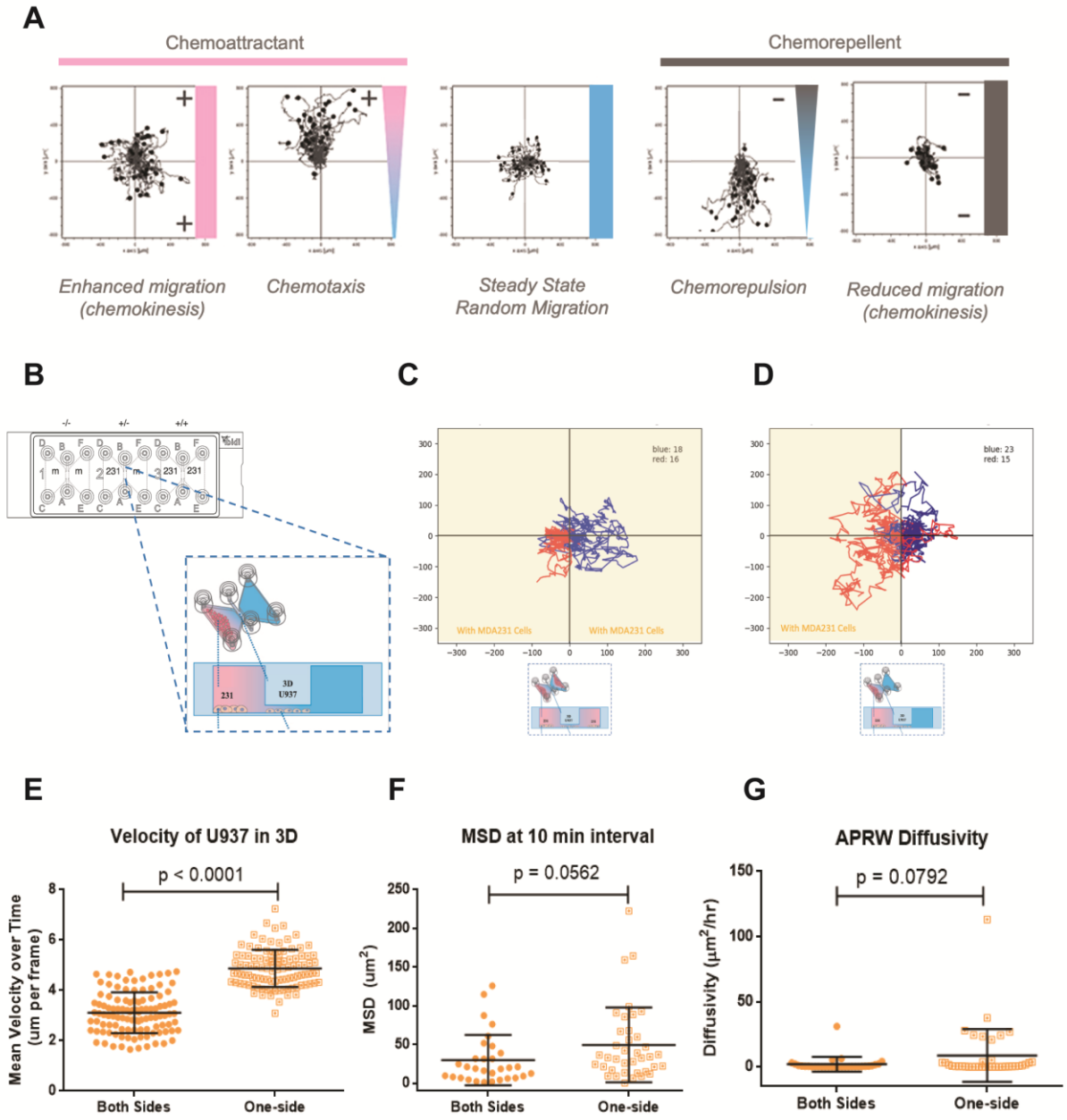

Figure 6. U937 Chemotaxis using µ-Slide

(A) Illustration of steady state and biased migrations.

(B) Illustration of experimental setup using ibidi® µ-slide chemotaxis system. Cancer cell secreted signaling molecules are shown in magenta, fresh media is shown in blue. U937 monocytes were seeded in the narrow channel between two chambers.

(C) U937 monocyte cell trajectories with cancer cells on both sides. Trajectories are normalized against individual cell start point.

(D) U937 monocyte cell trajectories with cancer cell on the left side. Trajectories are normalized against individual cell start point.
(E) Population average velocity as measured by distance traveled per frame. Mean and standard deviations are shown.
(F) Mean-squared displacement at 10 minute time lag for all cells. Mean and standard deviations are shown.
(G) Diffusivity as calculated by anisotropic persistent random walk model for all cells. Mean and standard deviations are shown.
Figures generated partially based on the online catalog of ibidi®. Unpaired t-test was performed.

3.3.2 BMDM Motility

Upon differentiation with PMA, U937 derived macrophages are not motile (data not shown). This is likely an artifact of cell line model and polarization conditions. Primary BMDMs were therefore used to study the macrophage motility capacities at various polarization states and in response to cancer conditions.

BMDMs were treated with cytokine or tumor conditioned media for about 24 hours before tracking started. This allows sufficient time for M1 and M2 phenotype to be stably polarized[90]. At a population level, M2 polarized macrophages are significantly more mobile than M1 polarized and naïve M0 BMDMs (Figure 7A, 7B, 8B). Neither high density nor low density KPC conditioned media had an effect on the MSD of BMDMs (Figure 7B).

Furthermore, for most of the conditions tracked, the MSD grows as a function of time lag (τ) with an exponent of 1 (i.e. MSD $\sim \tau^{\alpha}, \alpha = 1$), suggesting free diffusion (Figure 8A). The Gaussian distribution of probability density function of cell displacement (PDF-dR) is also consistent with random and PRW model (Figure 8C). The auto-correlation function of cell velocity (ACF) showed oscillation around zero, indicating where cell persistence time is less than that of time lag shown. For PRW and APRW statistics, ACF should show exponential decay with

time increments[88]. When the ACF is plotted for all the technical repeats for each condition, there is no clear exponential decay, suggesting BMDMs do not strictly follow PRW (Figure 8F).

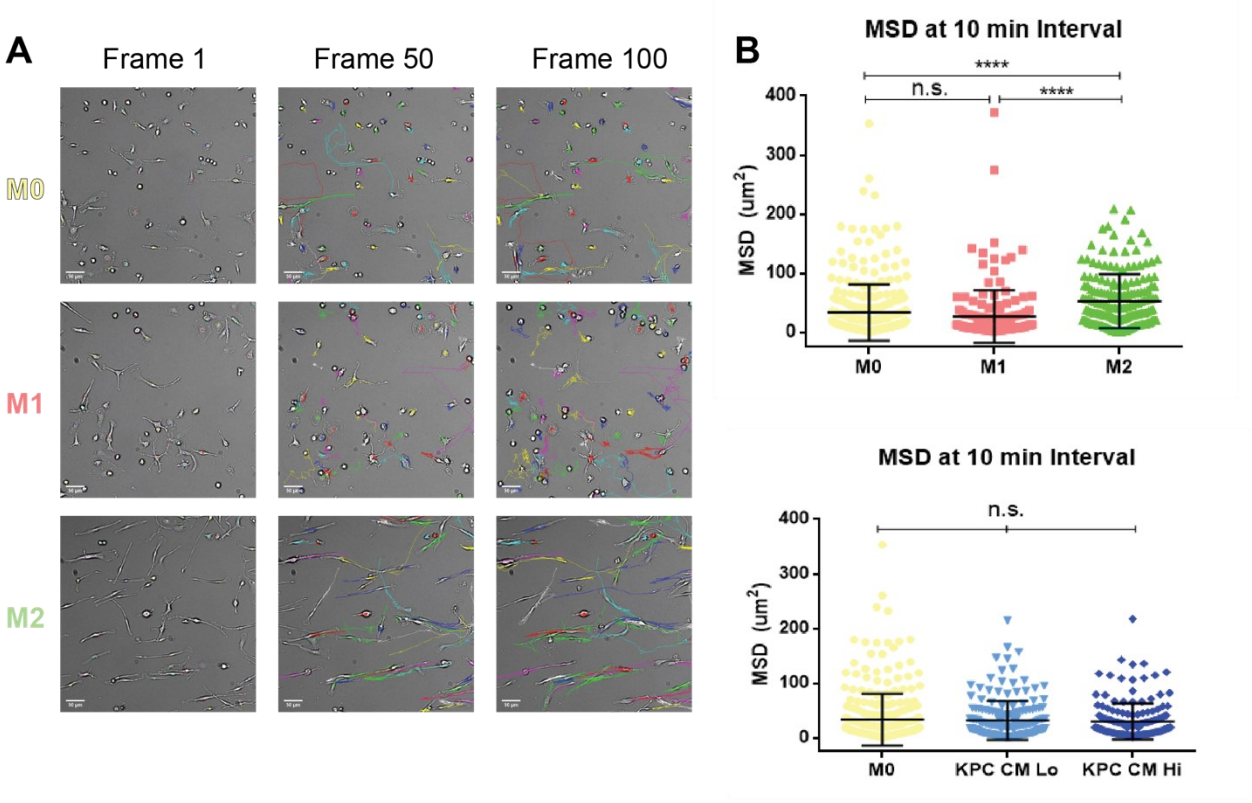

Figure 7. BMDM Motility Profiles

(A) BMDM cell trajectories at frame 1, 50, and 100. Frames are 10 minutes apart.
(B) Mean squared displacement for BMDMs. Calculations were done at 10 minute intervals.
n = 4 technical repeats for M0 condition, n = 3 technical repeats for all other conditions. Unpaired t-test was performed. n.s. = non-significant, $^{****}p < 0.0001$.

Consistent with the cell trajectories (Figure 8D – E), M0 naïve and M2 polarized BMDM motility profiles are more anisotropic. The velocity magnitude polarization profiles for M0 and M2 are more oval-like, whereas the M1 profile is more circular (Figure 8G), suggesting there is a predominate direction that these cells confer to while moving. KPC conditioned media treated cells

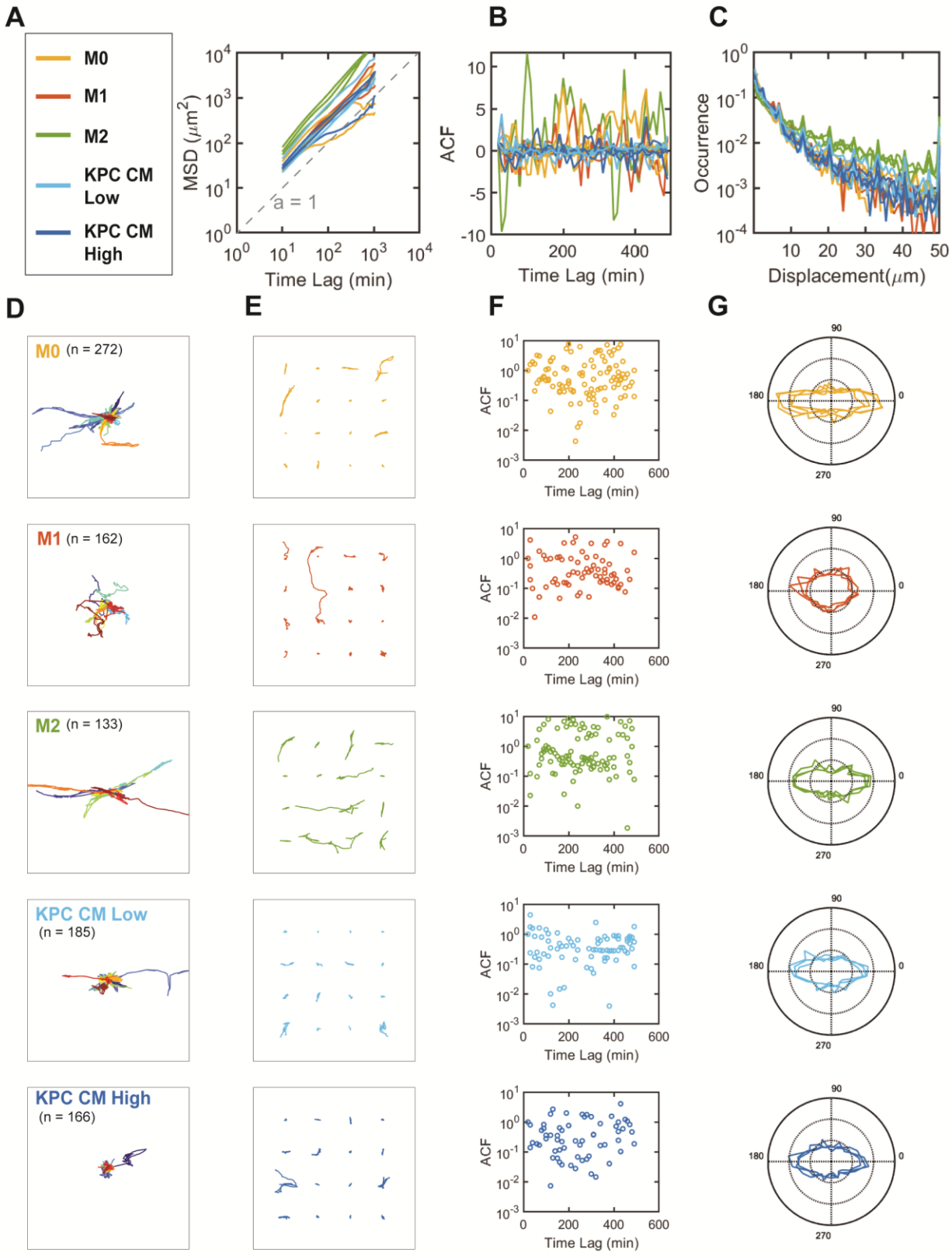
A
M0
M1
M2
KPC CM Low
KPC CM High
MSD (μm^2)
a = 1
Time Lag (min)
B
ACF
Time Lag (min)
C
Occurrence
Displacement(μm)
D
M0 (n = 272)
M1 (n = 162)
M2 (n = 133)
KPC CM Low (n = 185)
KPC CM High (n = 166)
E
F
ACF
Time Lag (min)
G
90
180
0
270

Figure 8. BMDM Motility Parameters by Condition

(A) Population averaged mean-squared displacement vs. time lag plot for all conditions.
(B) Auto-correlation function of cell velocities at different time lag. Linear scale.
(C) Probability density function of cell displacement.
(D) Cell trajectories normalized by start point. Box depicts a 400-μm square. n = total cell number.
(E) Cell trajectories of 16 randomly selected cells plotted on a 4x4 grid.
(F) Auto-correlation function of cell velocities at different time lag. Log scale.
(G) Velocity magnitude polarization profile for individual technical repeat. Primary axis of cell trajectory is aligned to x-axis, and non-primary axis of cell trajectory is aligned to y-axis.

The plots are composites of 4 technical repeats for M0 condition and 3 technical repeats for all others.

appear to be more polar than M1 phenotype as well, but their magnitudes of polarity cannot be distinguished between naïve M0 macrophages.

3.3.3 Motility Hierarchical Clustering

It was also found that within each condition, there are large amounts of cell-to-cell heterogeneity. To better understand the effects of polarization and cancer conditions, hierarchical clustering was performed for both spatial distribution of APRW parameters (Figure 9) and time dependent motility activity profile (Figure 10)[91].

For spatial clustering, persistence time for primary axis (Pp) and secondary axis (Pnp), diffusivity for primary axis (Dp) and secondary axis (Dnp), total diffusivity, anisotropy, and MSD at a short 10-minute time lag (MSD10) and a long 60-minute time lag (MSD60) were z-score normalized and used as clustering parameters. Trajectories from all conditions of BMDMs were pooled together and analyzed using MATLAB built-in ‘cosine’ distances and ‘ward’ linkages packages. Samples were iterated at different cluster numbers (Figure S2), and 6-cluster scheme was found to best explain observed trends (Figure 9A). For instance, if cluster P1 and P2 are compared, cluster P1 has markedly higher diffusivity and persistence along non-primary axis. P2 has higher anisotropy, or the ratio of diffusivities measured in primary and non-primary axis.

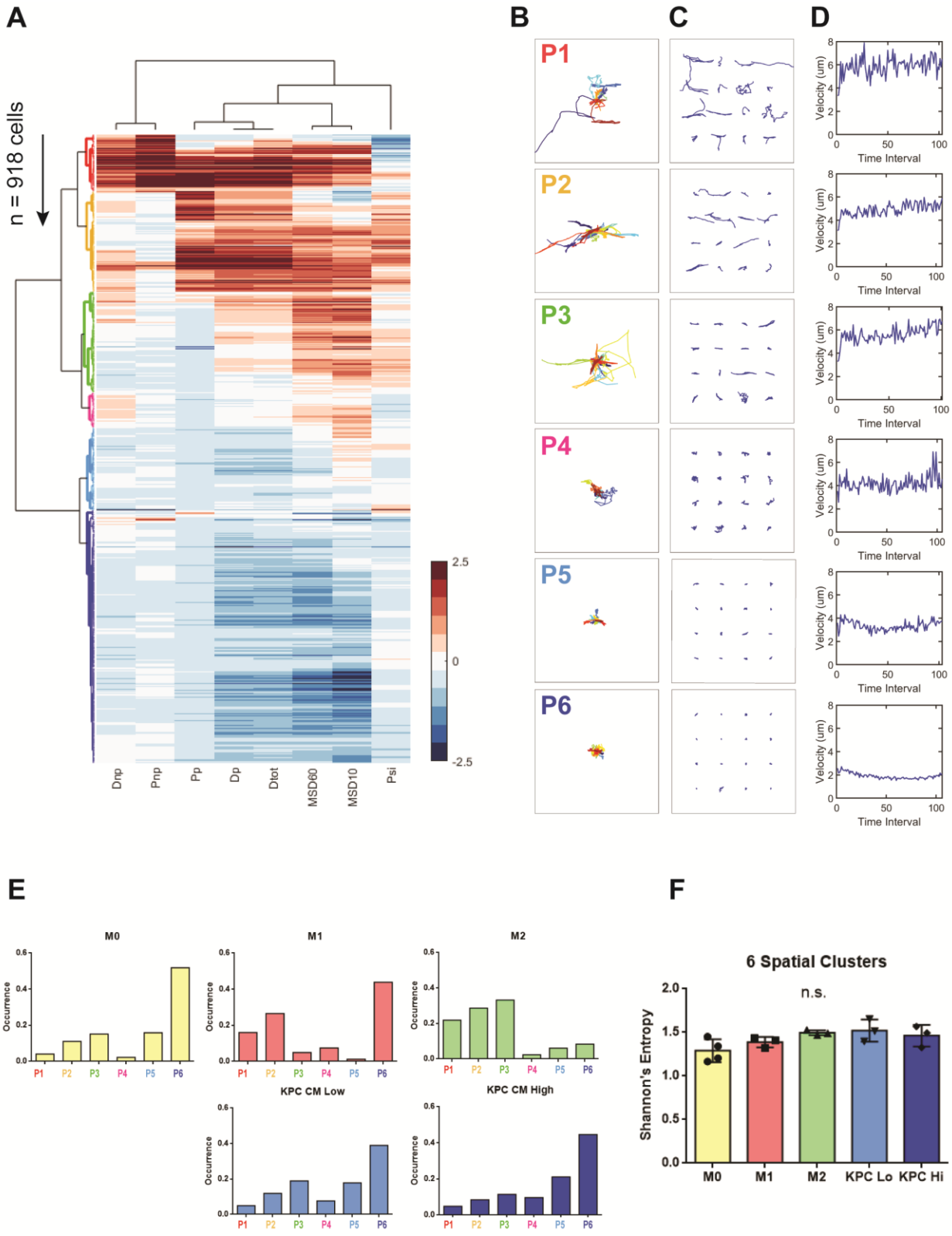
A
n = 918 cells
Dnp
Pnp
Pp
Dp
Dtot
MSD60
MSD10
Psi
2.5
0
-2.5
B
C
D
P1
P2
P3
P4
P5
P6
Velocity (um)
Time Interval
E
M0
M1
M2
KPC CM Low
KPC CM High
Occurrence
F
6 Spatial Clusters
n.s.
Shannon's Entropy
M0
M1
M2
KPC Lo
KPC Hi

Figure 9. BMDM Motility Clustering by Spatial Parameters

(A) Heatmap of z-score normalized BMDM motility parameters at single cell level. Dendrogram represents hierarchical clustering based on 'cosine' distances and 'ward' linkages. Each row represents a cell, each column represents the APRW parameter calculated for the 107 frames (17.8 hours) the cell was tracked. $D_{np,}$ diffusivity along non-primary axis of migration; $P_{np,}$ persistence time along the non-primary axis of migration; P_p, persistence time along the primary axis of migration; D_p, diffusivity along primary axis of migration; $D_{tot,}$ total diffusivity; MSD60, mean-squared displacement at 60 minute interval; MSD10, mean-squared displacement at 10 min interval; Psi, Anisotropy.
(B) Cell trajectories normalized against starting point, by cluster.
(C) Cell trajectories of 16 randomly selected cells plotted by cluster.
(D) Population average velocity vs frame of time. Velocity is measured by the distance traveled over the frame interval (10 min).
(E) Fractional abundance of cells within each cluster, plotted by condition.
(F) Shannon's entropy as a measure of heterogeneity. Calculated for each technical repeat.

Ordinary one-way ANOVA test ($\alpha = 0.05$) was performed with Tukey's multiple comparisons test. n.s. = non-significant.

This difference is fully captured in the cell trajectory plot (Figure 9B, 9C), where the P2 trajectories are flatter and more 1-dimensional in comparison to P1's.

Within the 6 clusters, cluster P1 has highest motility based on persistence, diffusivities, and MSDs. Cluster P6 is the least mobile, in fact, the trajectories showed almost no effective displacement of the 17 hours of tracking (Figure 9B, 9C). Velocity as measured by population average displacement per time frame is also consistent with the decreasing motility from P1 to P6 (Figure 9D). Furthermore, within each cluster, the motility is time invariant.

The fractional abundance of cells in each cluster is mapped out by condition (Figure 9E), and Shannon's entropy was calculated as a measure of heterogeneity (Figure 9F, Appendix B). Notably, M2 phenotype was previously observed as more motile than other conditions, here this increased motility is associated with high fractional abundance in fast moving clusters like P1, P2, and low abundance in slow moving clusters P4, P5, and P6. The overall cluster distribution of KPC conditioned media treated groups is similar to that of M0.

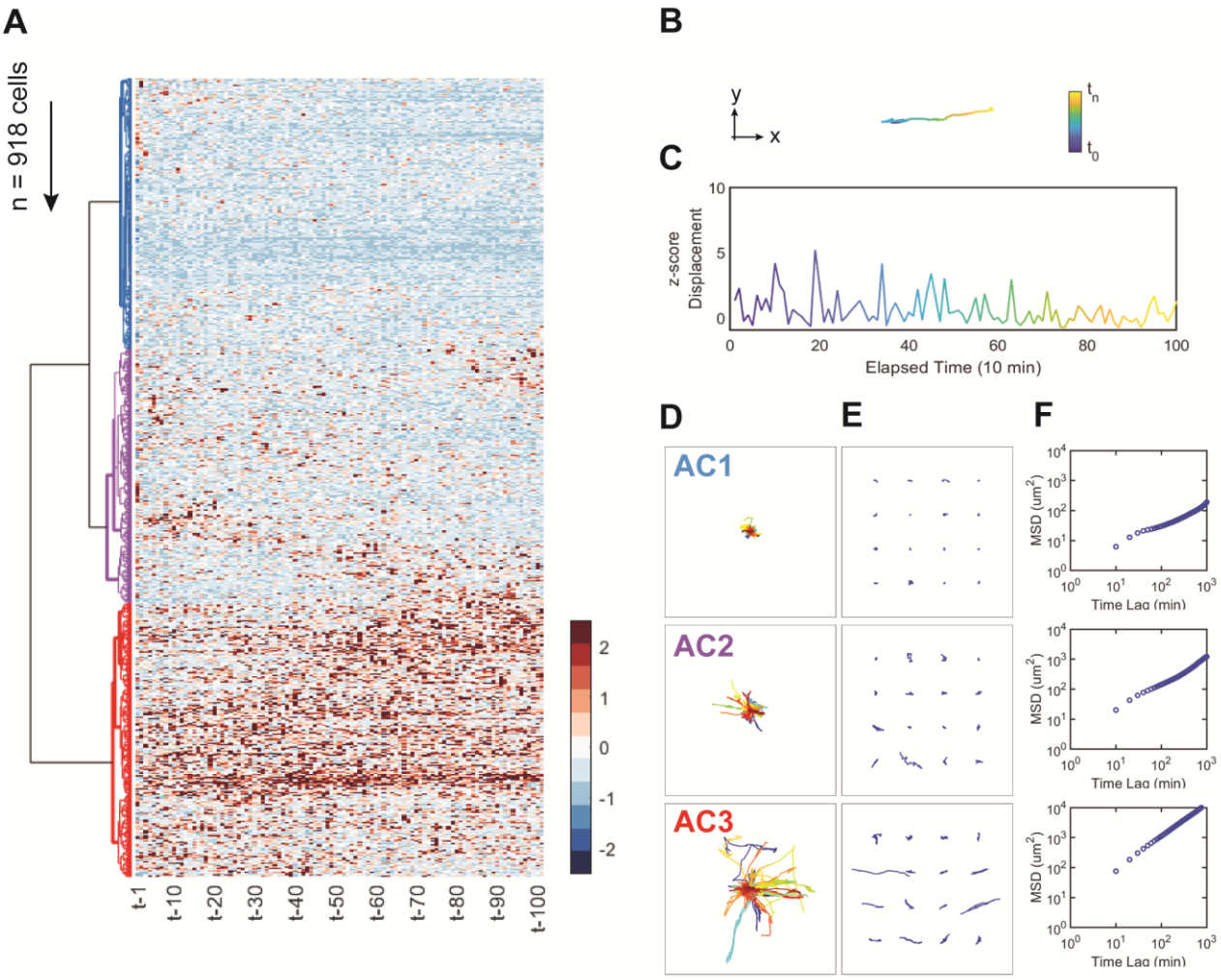
A
n = 918 cells
t-1
t-10
t-20
t-30
t-40
t-50
t-60
t-70
t-80
t-90
t-100
2
1
0
-1
-2
B
y
x
t_n
t_0
C
z-score Displacement
Elapsed Time (10 min)
D
AC1
AC2
AC3
E
F
MSD (um^2)
Time Lag (min)

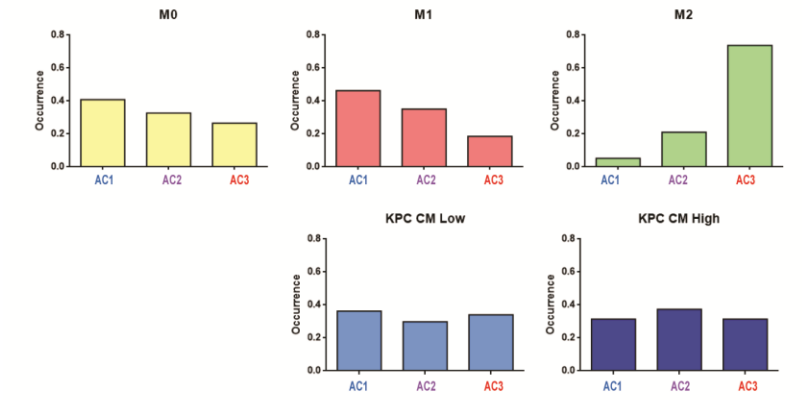
G
M0
M1
M2
KPC CM Low
KPC CM High
Occurrence
AC1
AC2
AC3

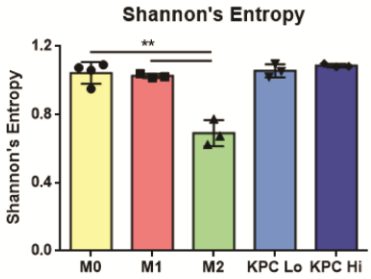
H
Shannon's Entropy
**
M0
M1
M2
KPC Lo
KPC Hi

Figure 10. BMDM Motility Clustering by Temporal Resolution

(A) Heatmap of z-score normalized 1-D displacement at single cell level. Dendrogram represents hierarchical clustering based on 'cosine' distances and 'ward' linkages. Each row represents a cell, each column represents a frame tracked. Two sequential frames are 10 minutes apart.
(B) Example of a cell trajectory with respect to time. Initial time frame is shown in blue, final time frame is shown in yellow.
(C) 1-D displacement vs time plot of the same cell shown in (B), termed (motility) activity profile here.
(D) Cell trajectories normalized against starting point, plotted by activity cluster.
(E) Cell trajectories of 16 randomly selected cells.
(F) Mean-squared displacement vs time lag, plotted by activity cluster.
(G) Fractional abundance of cells within each activity cluster, plotted by condition.
(H) Shannon's entropy as a measure of heterogeneity. Calculated for each technical repeat.
Unpaired t test was performed. $^{**}p < 0.01$.

Single cell BMDM motility data was also clustered based on the activity profile (i.e. the distance traveled per cell per frame) over the course of tracking. For individual cells, the 2D x, y-trajectories were converted to 1D distance (Appendix B). The activity profile of the cell can then be generated based on 1D distance at each time frame (Figure 10B, 10C). Three activity clusters (ACs) were generated to optimally classify the BMDM data. AC1 represents cells that were not moving, AC2 represents cells with transient and marginal movements, and AC3 represents cells with highest motilities (Figure 10D – F).

Once again, M2 BMDMs had high fractional abundance in the most motile cluster AC3, and low abundance in the least motile cluster AC1 (Figure 10G). Since about 70% of M2 cells were in AC3, M2 distribution is highly skewed (more homogeneous), and therefore has the lower Shannon's Entropy (Figure 10H).

3.4 Discussion

Whether it is directed chemotaxis, or uniform chemokinesis, motility is essential for macrophage function. Here we demonstrated that MDA-MB-231 cancer cells are capable of

modulating monocyte motility using U937 cell line model. While the exact mechanisms remain to be elucidated, cancer cell mediated reduction of immune cell motility has significant implications on immune evasion. Using primary bone marrow derived macrophages, it is clear that M2 cytokine polarized macrophage are more motile. Although in these studies, no significant differences were observed for BMDM motility of cancer conditioned media treated group and M0 naïve group, it is still possible for cancer cells to modulate macrophage motility.

A variety of factors could be responsible for these negative result. For instance, the tracking time interval could be too long to capture the transient motility features, the KPC cancer cells could lack specific signaling molecules, or the concentration of signaling factors are not produced to sufficient levels. Two densities of cancer cells were explored here in an attempt to capture the autocrine signaling process that is important for tumorigenesis. However, no apparent differences were observed between the high and low density conditioned media. It is possible these seeding densities still did not incorporate the pathologically relevant range, or the stiff substrate of tissue culture dish inactivated expressions of many important signaling molecules[92].

Chapter 4 – **Macrophage Phenotypes**

4.1 Introduction

Macrophages are highly plastic and can be polarized into a range of phenotypes (Figure 2). While tumor associated macrophages do not confer to steady state phenotypes, they carry out vast pathological functions. It has been demonstrated that morphology of the macrophage can modulate its phenotype. Specifically, using an engineered substrate to form elongated cells can promote M2-like expression profiles[93]. It is perceivable that the phenotype of macrophages can in turn be predicted by its morphology. Indeed, Rostam and colleagues have demonstrated the feasibility of accurately distinguishing M1 and M2 macrophages from DNA and actin stained fluorescent microscopy images using machine learning[94].

Here we aim to elucidate if cancer conditioned media can polarize macrophages to distinct phenotypes as suggested by mRNA expression and morphology. MDA-MB-231 cancer conditioned media were used to treat U937 monocyte cell line derived macrophage, and KPC conditioned media were used to treat primary mouse BMDMs. Two seeding densities were used to generate cancer conditioned media.

4.2 Materials & Methods

4.2.1 U937 Derived Macrophages

For RNA extraction, U937 cells were seeded in a 6 well plate at $0.3{\sim}0.6 * 10^6$ cells per well. Complete RPMI media (RPMI-1640 with 10% HI-FBS, 1% P/S, 1% HEPES, and 1% L-Glu)

containing 1 μM Phorbl 12-myristate 13-acetate (PMA) (Sigma-Aldrich) were used to induce U937 differentiation into macrophage. On day 3, PMA containing supernatant is aspirated, and the cells were washed with PBS. Complete RPMI containing 50 ng/mL IFN- γ and 100 ng/mL LPS were added for M1. 50 ng/mL IL-4 and 50 ng/mL IL-13 were added for M2, and fresh media were added for M0. Cells were harvested on day 5. This differentiation protocol is based on published references[95–97]. The concentrations of PMA and polarizing cytokines were modified, and no apparent adverse effects were observed with these elevated concentrations.

4.2.2 Generation of MDA Conditioned Media

MDA-MB-231 conditioned media were generated same as the KPC conditioned media (Section 3.2.4). At the time of treatment, conditioned media were added to equal volume of fresh media in order to prevent nutrient starvation.

4.3 Results

4.3.1 U937 Derived Macrophage

U937 derived macrophages exhibited few morphological differences upon polarization. It is not readily possible to distinguish cancer conditioned media treated macrophages based on manual classification alone (data not shown).

High density MDA-MB-231 conditioned media treated macrophages showed a significant upregulation of TNF-α, as well as suppressions of CXCL10 and IL1β when compared to naïve M0 macrophages (Figure 11). Interestingly, only TNF-α trend is conserved in low cancer cell density

conditioned media treatment. This suggests the MDA-MB-231 cells can potentially modulate macrophage behavior differentially during different stages of tumor progression, although varying seeding density is an extremely simplified attempt to capture autocrine signaling changes during tumorigenesis.

CXCL10 is a chemokine ligand, and its binding can modulate adhesion and T cell migration. IL-1β is a proinflammatory cytokine that can facilitate T cell activation. Overall, the high seeding density MDA-MB-231 conditioned media appears to be promoting cancer escape, although TNF-α has been shown to both promote and suppress tumor growth[98].

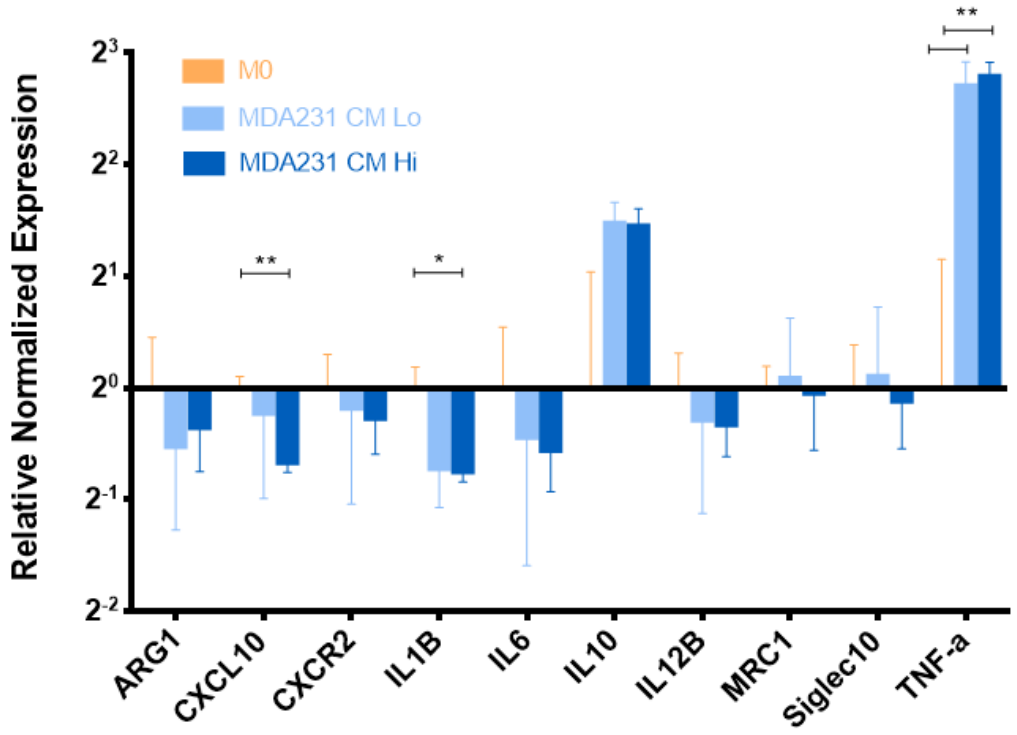

Figure 11. U937 Derived Macrophage Polarization Profile

RT-qPCR quantification of selective macrophage genes for U937 derived macrophages. B-actin and TBP were used as reference genes. The expression was normalized against M0 naïve macrophage. 2 biological repeats were used for M0, 3 biological repeats were used for MDA231 conditioned media groups. Two – way ANOVA test ($\alpha = 0.05$) was performed with Tukey's multiple comparisons test. Unless specified, all pairs are non-significant. $^{*}p < 0.05$, $^{**}p < 0.01$.

4.3.2 Bone Marrow Derived Macrophages

BMDMs exhibited 3 distinct morphologies: elongated, round, and fibroblast-like (Figure 12A). Time-lapse images showed these morphologies are stable for hours, and round cell shapes do not appear to be caused by cell death or division. Upon cytokine induced polarization, M1 BMDMs are significantly enriched in round cell shape, and M2 BMDMs are enriched in elongated morphology (Figure 12B). KPC conditioned media treated groups did not show as drastic enrichments like that of cytokine treated. However, both low density and high density KPC conditioned media had different morphology profiles when compared to M0 (Figure 12C). Specifically, conditioned media reduce the fractional abundance of round cells and increase the abundance of fibroblast like cells.

Furthermore, clustering analysis of mRNA data suggested these KPC CM treated cells are more M0 like, rather than M1 or M2-like. However, Ptgs1 which mediates the biosynthesis of prostaglandins and promotes angiogenesis is similarly upregulated in KPC CM treated and M2 BMDMs. Interestingly, CM from a higher seeding density of KPC can induce different expression of 18s, Hprt, S100A4, and Cfd, which suggests potential roles in regulating translation, biosynthesis, differentiation, and complement activation.

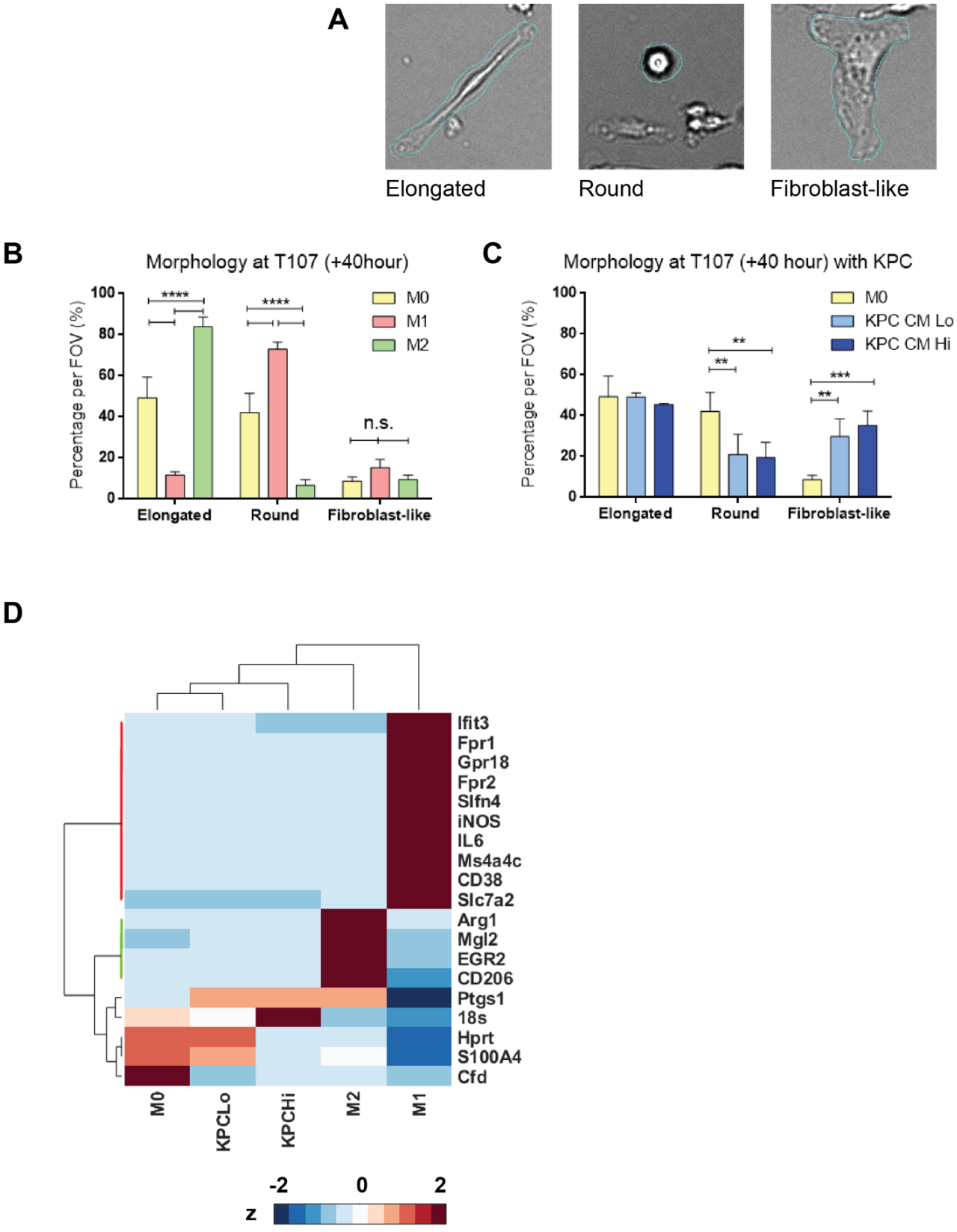
A
Elongated
Round
Fibroblast-like
B
Morphology at T107 (+40hour)
Percentage per FOV (%)
M0
M1
M2
****
****
n.s.
Elongated
Round
Fibroblast-like
C
Morphology at T107 (+40 hour) with KPC
Percentage per FOV (%)
M0
KPC CM Lo
KPC CM Hi
**
**
***
**
Elongated
Round
Fibroblast-like
D
Ifit3
Fpr1
Gpr18
Fpr2
Slfn4
iNOS
IL6
Ms4a4c
CD38
Slc7a2
Arg1
Mgl2
EGR2
CD206
Ptgs1
18s
Hprt
S100A4
Cfd
M0
KPCLo
KPCHi
M2
M1
-2
0
2
z

Figure 12. BMDM Phenotype

(A) Representative bright field images of the three types of BMDM morphology
(B) Fractional abundance of cells in each morphology, cytokine polarized groups vs control. n = 4 technical repeats.
(C) Fractional abundance of cells in each morphology, KPC conditioned media treated groups. n = 4 technical repeats M0, n = 3 technical repeats for others.
(D) Heatmap of mRNA expression quantified by RT-qPCR. B-actin and RPL13A were used as reference genes. The expressions were z-score normalized for each gene target across all conditions. Red and green bars in the dendrogram represent M1 associated and M2 associated gene clusters respectively.

Two – way ANOVA test ($\alpha = 0.05$) was applied with Tukey's multiple comparisons test. Unless specified, all pairs are non-significant. n.s. = nonsignificant, $^{**}p < 0.01$, $^{***}p < 0.001$, $^{****}p < 0.0001$.

4.4 Discussion

Conditioned media provides a simplified system to study paracrine signaling in cancer conditioned media. For U937 derived macrophages, MDA-MB-231 CM functions differently at different cancer seeding density. At low density, CMs treated macrophages have a more M0-like gene expression profile. At high density, markers responsible for tumor promotion start to appear. This is further supported in KPC – BMDM study, although some exceptions are present.

In BMDMs, CMs can also alter macrophages morphology distributions, although it is not clear if the morphological changes shown are related to any molecular or functional change.

Chapter 5 – **Final Remark**

Macrophages have been shown to infiltrate both primary sites and metastatic niches during tumorigenesis. Their role in maintaining tumor growth and immune evasion poses a serious clinical challenge. Here we speculated the origin of these macrophages and investigated cancer cells' effect on macrophage recruitment, motility, morphology, and mRNA expression. While it is not yet clear how cancer conditions modulate macrophage motility, significant changes were seen for macrophage morphology and gene expression.

These are no doubt only a tip of the cancer immunomodulatory iceberg. Some of the key questions are still left unanswered. For starters, what signals are used to recruit macrophages, what signals are suppressing the pro-inflammatory activities, and what signals regulate the switch between early stage modulation and late stage modulation?

From an assay development perspective, if the macrophage morphology can be correlated with its motility and gene expression, it would be a beneficial predictor of tumor conditioning.

Overall, mechanistic insights into the recruitment and polarization of tumor associated macrophages would open new possibilities for cancer immunotherapy.

Chapter 6 – **General Materials & Methods**

6.1 Solutions and Buffers

Table 2. Stock Solution Formulation

	Stock Solution/Buffer	Formulation
6.1.1	FACS Wash Buffer	2% FBS, 0.1% Sodium Azide in 1x PBS pH 7.4
6.1.2	FACS Fixation Buffer	1.6% PFA, 2% Glucose, 0.1% Sodium Azide in 1x PBS pH 7.4
6.1.3	Fixation & Permeabilization Buffer	2% FCS, 1.6% PFA, 0.1% Sodium Azide, 0.01% Saponin in PBS pH 7.4
6.1.4	FACS Permeabilization Buffer	2% FBS, 0.1% Sodium Azide, 0.01% Saponin in 1x PBS pH 7.4

6.2 Cell Culture

6.2.1 Serum Heat Inactivation

Fetal Bovine Serum (Corning) used for macrophage maintenance and experiments was heat inactivated to prevent unintended activation. The serum was heated to 56 °C for 30 minutes, which is consistent with the heat inactivation protocol used by the manufacturer.

6.2.2 Suspension Cells

THP-1 and U937 cell lines were grown in suspension in RPMI-1640 media (Gibco) containing 10% Heat-Inactivated Fetal Bovine Serum (Corning) (HI-FBS), 1% Pen Strep (Gibco), 1% L-glutamine (200mM) (Gibco), 1% HEPES (1M) (Gibco). The cell cultures were incubated at 37 °C with 5% CO_2 and humidification. The cell lines were maintained at a density of less than $1.2 * 10^6$ cell/mL and a passage number of less than 25 generations.

6.2.3 Adherent Cells

MDA-MB-231, KPC and KPC Luc^+ GFP^+ cell lines were maintained in T-75 flasks with DMEM (Corning 10-013-CV formulation) containing 10% HI-FBS and 1% Pen Strep. KPC and KPC Luc^+ GFP^+ cells are generous gifts from Dr. Adrian Murphy and Dr. Elizabeth Jaffee. These cells originated from murine spontaneous cancer model of PDAC[77]. The adherent cells were maintained below confluency as indicated by visual inspection. The cell lines were kept at 37 °C with 5% CO_2 and humidification.

6.4 Real Time qPCR

6.4.1 RNA Extraction

For U937 derived macrophages and BMDMs, cells were seeded in 6-well plate. Upon polarization or treatment, media was aspirated and the cells were washed using PBS without

calcium and magnesium (Coring). Then 0.5 mL of TRIzol reagent (Invitrogen) were added to each well. Once cells are completely lysed, equal volume of 200 proof ethanol was added to each well. The samples are then kept on ice and immediately purified.

RNA purification was done using Direct-zol RNA Kit (Zymo Research) following manufacturer's guidelines. In short, the RNA lysate was passed through spin columns (Genesee Scientific) by centrifugation at 14,000 RPM for 30 seconds using a tabletop centrifuge. The flow through was collected and disposed. RNA bound columns were washed twice with 400 µL Direct-zol RNA PreWash buffer (Zymo Research) each time, then once with 700 µL RNA Wash Buffer (Zymo Research). The column was then dried by centrifugation at 14,000 RPM for 2 minutes. The RNA was then triple eluted with 20 µL of molecular biology grade water (Quality Biological) by collecting the flow-through and replacing it on top of column. RNA samples were immediately quantified and reverse transcribed.

6.4.2 Reverse Transcription

RNA quality and quantity were assigned using ND-1000 Spectrophotometer (NanoDrop). RNA was then reverse transcribed using iScript cDNA Synthesis kit (Bio-Rad) according to manufacturer's instructions. In short, 1 µg of RNA and water were added to 4 µL of 5x iScript Reaction Mix and 1 µL of reverse transcriptase to constitute a total reaction volume of 20 µL in a 200 µL PCR tube.

6.4.3 Quantitative PCR

Real Time qPCR was performed using 384-well plates (Bio-Rad) and Real Time Detection System (Bio-Rad, CFX384). Each well contains 1.5 µL of cDNA, 0.5 µL of primer mix, 3 µL water, and 5 µL of SYBR Green Master Mix (Bio-Rad). 4 technical repeats were performed for each target/condition pair.

6.4.4 qPCR Data Processing

qPCR data were exported as .zpcr files. The data were then subsequently processed using Bio-Rad CFX Manger version 3.1.

6.5 Flow Cytometry

6.5.1 Fluorophore Panel Design

Fluorophore panels were designed using Fluorescence SpectraViewer (Thermo Fisher) and FluoroFinder to minimize spectral overlap. Fluorophores were further selected to be compatible with the BD FACSCanto cytometer.

6.5.2 Sample Preparation

Cells were detached by incubating in TrypLE Express Enzyme (Gibco) at 37 °C. The detached cells are further dissociated, washed, and pelleted in a 15 mL conical tube. The supernatant was discarded. $0.3 - 0.75 * 10^6$ cells were used for each sample. For macrophage

staining, Fc receptors were first blocked by adding 5 µL of TruStain FcX (anti-mouse CD16/32 or human Fc Receptor Blocking solution, BioLegend) to the pellet and residual volume. The samples were then vortexed and incubated at room temperature for 15 minutes. Surface antigen targeted antibodies were then diluted in FACS Wash Buffer (Section 6.1.1) according to manufacturer's recommended concentrations. Staining solution was directly added to the FcX blocked samples and incubated at 4°C for 30 minutes. Upon incubation, 3 mL of FACS wash buffer was then added to each sample for washing. Cells were pelleted and supernatant was discarded. Samples were then suspended in 0.35 mL of FACS wash buffer unless fixation is needed for delayed analysis or subsequent intracellular staining.

To fix the stained cells for analysis at another time, 0.35 mL of FACS fixation buffer (Section 6.1.2) was added instead of wash buffer.

For intracellular staining with EGR2, cells were fixed in Fixation & Permeabilization Buffer (Section 6.1.3) at 4°C for 40 minutes. The cells were then spun down and washed with permeabilization buffer (Section 6.1.4) for 3 times before incubating with intracellularly targeted antibodies at manufacturer's recommended concentration and 4°C for 45 minutes. After pelleting and washing with FACS Permeabilization Buffer for 3 times, the cells were resuspended in FACS wash buffer.

Table 3. List of Flow Cytometry Antibodies

Antigen	**Isotype**	**Species**	**Fluorophore**	**Clone**	**Manufacturer**	**Notes**
CD11b (mouse)	IgG2b, kappa	Rat	Alexa Fluor 647	M1/70	BioLegend	Alpha M Integrin, Pan Macrophage Marker
F4/80 (Mouse)	IgG2a, kappa	Rat	APC / Cyanine 7	BM8	BioLegend	Epidermal Growth Factor TM7

						family, Pan Macrophage Marker
CD38 (Mouse)	IgG2a, kappa	Rat	PE/Cy7	90	BioLegend	T10, used as M1 Marker[90]
EGR2 (Mouse)	IgG2a, kappa	Rat	Alexa Fluor 488	erongr2	ThermoFisher	Early growth response 2, used as M2 Marker[90]
CD11b (Human)	IgG1, kappa	Mouse	PE	ICRF44	BioLegend	Integrin alpha M chain, Pan Macrophage Marker
CD14 (Human)	IgG2a, kappa	Mouse	APC	M5E2	BioLegend	LPS receptor, Pan Monocyte Marker
CD86 (Human)	IgG2b, kappa	Mouse	PE/Cy5	IT2.2	BioLegend	B7-2, costimulatory molecule
CD206 (Human)	IgG1, kappa	Mouse	PE/Cy7	15-2	BioLegend	MRC1, Macrophage Mannose Receptor, used to delineate monocyte from Macrophage
HLA-DR (Human)	IgG2a, kappa	Mouse	APC/Cy7	L243	BioLegend	MHC Class II, used to characterize macrophage activation

6.5.3 Compensation Controls

To prepare single color compensation control, 3 μL of antibody was added to 1 drop of OneComp eBeads (ThermoFisher) and 300 μL of FACS Wash Buffer.

To prepare unstained control groups, the cells were harvested and incubated at the same conditions as that of antibody labeled samples, with an exception that no label or FACS wash buffer were added where appropriate.

6.5.4 Equipment Calibration

The stained samples were analyzed using BD FACSCanto located at the Johns Hopkins Integrated Imaging Center. The cytometer was maintained by the core facility, and calibrated with FACSDiva CS&T Research Beads (BD) before each use. The data were exported as .fcs files and analyzed using FlowJo 10.6.1.

6.6 Microscopy

6.6.1 Equipment

Florescence and bright field images were taken on a Nikon Ti-E microscope equipped with a motorized stage (Nikon), a Perfect Focus System (Nikon), a Lambda SC shutter controller (Sutter Instrument), and an Andor camera with a 10x magnification objective (Nikon S Fluor; numerical aperture, 0.5). For live cell imaging, the microscope stage is humidified, and its environmental conditions were kept at 37 °C and 5% CO_2 with a stage top live cell box (Tokai Hit, model INU). For high magnification fluorescence imaging, a 60x oil immersion objective with apochromatic and flat field aberration correction (Nikon; Numerical aperture, 1.4).

6.6.2 Motility Sample Preparation

Cells were seeded at 2,000 or 3,000 cells per 75 μL per well onto a 96-well tissue culture treated 96-well assay plate (Corning, costar 3603). Bordering wells were filled with PBS to minimize the edge well effects caused by differential evaporation rate across the plate. After cell

attachment overnight, the plate was mounted on the microscope stage. Bright field images were recorded at every 10 min for 17 hours.

BMDM cells were seeded on 96-well untreated high performance glass plate (Cellvis P96-1.5H-N) for motility tracking and subsequent high magnification fluorescence imaging.

6.6.3 Fluorescence Sample Preparation

Cells were seeded at 3,000 or 5,000 cells per 75 µL per well onto a 96-well plate. Bordering wells were filled with PBS to minimize the edge well effects caused by differential evaporation rate across the plate. Upon attachment and treatment, media were aspirated using a multichannel pipette. Cells were fixed with 50 µL of 4% PFA per well at room temperature for 15 minutes, then washed with equal volume of PBS for 3 times. The samples were then stained with Hoechst 33342 (Thermo Fisher) at 2 µg/mL and Alexa Fluor 568 Phalloidin (Invitrogen) at 1/500 of stock solution (or approximately 130 nM) in 50 µL of PBS per well. Upon 1 hour incubation in dark, the staining solution was aspirated and the cells were washed with PBS for 3 times. Then 75 µL of PBS was added to each well, and the plate is mounted on the microscope stage for imaging.

6.6.4 Microscopy Data Processing

The microscopy imaging was registered in NIS Elements software (Nikon), and exported as .tif files.

6.7 Analysis Software

6.7.1 FIJI Cell Motility Tracking

Time course images were loaded into Fiji ImageJ as an image sequence[99]. Individual cell trajectories were registered using Manual Tracking plugin. Coordinate data were then exported as .csv files, which need to subsequently parsed for analysis using MATLAB.

6.7.2 FlowJo

All flow cytometry data were analyzed using FlowJo 10.6.1 under the academic license with Johns Hopkins Integrated Imaging Center.

6.7.2 Excel Parsing

.csv tracking files were parsed to remove header, convert X-, Y- positions to the unit of μm instead of pixel, and outputted as a .xlsx file. Excel parsing was done using a simple custom python script.

6.7.3 Motility Clustering

Anisotropic Persistent Random Walk (APRW) model was used to fit the motility tracking data. The MATLAB script for the APRW parameter calculations were edited from a published

protocol[88]. A driver function was written for the purpose of this study. The hierarchical clustering script was written based on prior work published in BioRxiv[91].

All analysis scripts are available on GitHub repository under MIT license for open access (Wirtz-Lab/ HX_Motility_HierarchicalClustering).

6.8 Figure Illustrations

6.8.1 BioRender

Figure 1, Figure 4, and Figure 5A were created with *BioRender.com* under an individual academic license.

6.8.2 GraphPad Prism 6

Column graphs and statistical tests were generated in GraphPad.

6.8.3 Adobe Illustrator

Figures were edited and complied using Adobe Illustrator 2020.

References

1. Harris, M. Development of an Optogenetic Toolkit for the Interrogation of T cell Signalling Dynamics. (University of Cambridge, 2018). doi:10.17863/CAM.21363
2. Chaplin, D. D. Overview of the immune response. *J. Allergy Clin. Immunol.* **125**, S3–S23 (2010).
3. Yan, N. & Chen, Z. J. Intrinsic antiviral immunity. *Nat. Immunol.* **13**, 214–222 (2012).
4. Thaiss, C. A., Zmora, N., Levy, M. & Elinav, E. The microbiome and innate immunity. *Nature* **535**, 65–74 (2016).
5. Senovilla, L., Galluzzi, L., Zitvogel, L. & Kroemer, G. Immunosurveillance as a regulator of tissue homeostasis. *Trends Immunol.* **34**, 471–481 (2013).
6. Dunkelberger, J. R. & Song, W.-C. Complement and its role in innate and adaptive immune responses. *Cell Res.* **20**, 34–50 (2010).
7. Murray, P. J. & Wynn, T. A. Protective and pathogenic functions of macrophage subsets. *Nat. Rev. Immunol.* **11**, 723–737 (2011).
8. Takeda, K. & Akira, S. Toll-like receptors in innate immunity. *Int. Immunol.* **17**, 1–14 (2005).
9. Blum, J. S., Wearsch, P. A. & Cresswell, P. Pathways of antigen processing. *Annu. Rev. Immunol.* **31**, 443–473 (2013).
10. Beutler, B. Innate immunity: an overview. *Mol. Immunol.* **40**, 845–859 (2004).
11. Elhanati, Y., Murugan, A., Callan, C. G., Mora, T. & Walczak, A. M. Quantifying selection in immune receptor repertoires. *Proc. Natl. Acad. Sci.* **111**, 9875 LP – 9880 (2014).
12. Rajewsky, K. Clonal selection and learning in the antibody system. *Nature* **381**, 751–758 (1996).

13. Klein, L., Hinterberger, M., Wirnsberger, G. & Kyewski, B. Antigen presentation in the thymus for positive selection and central tolerance induction. *Nat. Rev. Immunol.* **9**, 833–844 (2009).

14. Luckey, C. J. *et al.* Memory T and memory B cells share a transcriptional program of self-renewal with long-term hematopoietic stem cells. *Proc. Natl. Acad. Sci. U. S. A.* **103**, 3304 LP – 3309 (2006).

15. Kurosaki, T., Kometani, K. & Ise, W. Memory B cells. *Nat. Rev. Immunol.* **15**, 149–159 (2015).

16. Mueller, S. N., Gebhardt, T., Carbone, F. R. & Heath, W. R. Memory T Cell Subsets, Migration Patterns, and Tissue Residence. *Annu. Rev. Immunol.* **31**, 137–161 (2013).

17. Netea, M. G. *et al.* Trained immunity: A program of innate immune memory in health and disease. *Science (80-.).* **352**, 427 (2016).

18. Lau, C. M. *et al.* Epigenetic control of innate and adaptive immune memory. *Nat. Immunol.* **19**, 963–972 (2018).

19. Monie, T. P. Section 1 - A Snapshot of the Innate Immune System. in (ed. Monie, T. P. B. T.-T. I. I. S.) 1–40 (Academic Press, 2017). doi:https://doi.org/10.1016/B978-0-12-804464-3.00001-6

20. Taylor, P. R. *et al.* Macrophage Receptors and Immune Recognition. *Annu. Rev. Immunol.* **23**, 901–944 (2004).

21. Józefowski, S., Sulahian, T. H., Arredouani, M. & Kobzik, L. Role of scavenger receptor MARCO in macrophage responses to CpG oligodeoxynucleotides. *J. Leukoc. Biol.* **80**, 870–879 (2006).

22. Rőszer, T. Understanding the Mysterious M2 Macrophage through Activation Markers and

Effector Mechanisms. *Mediators Inflamm.* **2015**, 816460 (2015).

23. Ley, K., Pramod, A. B., Croft, M., Ravichandran, K. S. & Ting, J. P. How Mouse Macrophages Sense What Is Going On. *Front. Immunol.* **7**, 204 (2016).
24. Schmid, M. C. *et al.* Integrin CD11b activation drives anti-tumor innate immunity. *Nat. Commun.* **9**, 5379 (2018).
25. Shi, J., Mcintosh, R. S. & Pleass, R. J. Antibody- and Fc-receptor-based therapeutics for malaria. *Clin. Sci.* **110**, 11–19 (2005).
26. Barkal, A. A. *et al.* CD24 signalling through macrophage Siglec-10 is a target for cancer immunotherapy. *Nat. lettter* **10**, (2019).
27. Chao, M. P., Weissman, I. L. & Majeti, R. The CD47-SIRPα pathway in cancer immune evasion and potential therapeutic implications. *Curr. Opin. Immunol.* **24**, 225–232 (2012).
28. Le Cabec, V., Carréno, S., Moisand, A., Bordier, C. & Maridonneau-Parini, I. Complement Receptor 3 (CD11b/CD18) Mediates Type I and Type II Phagocytosis During Nonopsonic and Opsonic Phagocytosis, Respectively. *J. Immunol.* **169**, 2003 LP – 2009 (2002).
29. Pathria, P., Louis, T. L. & Varner, J. A. Targeting Tumor-Associated Macrophages in Cancer. *Trends Immunol.* **40**, 310–327 (2019).
30. Lavin, Y., Mortha, A., Rahman, A. & Merad, M. Regulation of macrophage development and function in peripheral tissues. *Nat. Rev. Immunol.* **15**, 731–744 (2015).
31. Varol, C., Mildner, A. & Jung, S. Macrophages: Development and Tissue Specialization. *Annu. Rev. Immunol.* **33**, 643–675 (2015).
32. Ginhoux, F. & Jung, S. Monocytes and macrophages: developmental pathways and tissue homeostasis. *Nat. Rev. Immunol.* **14**, 392–404 (2014).
33. Chávez-Galán, L., Olleros, M. L., Vesin, D. & Garcia, I. Much More than M1 and M2

Macrophages, There are also CD169+ and TCR+ Macrophages . *Frontiers in Immunology* **6**, 263 (2015).

34. Mosser, D. M. & Edwards, J. P. Exploring the full spectrum of macrophage activation. *Nat. Rev. Immunol.* **8**, 958–969 (2008).

35. Xue, J. *et al.* Transcriptome-based network analysis reveals a spectrum model of human macrophage activation. *Immunity* **40**, 274–288 (2014).

36. Graney, P. L. *et al.* Macrophages of diverse phenotypes drive vascularization of engineered tissues. *Sci. Adv.* **6**, eaay6391 (2020).

37. O'Rourke, S. A., Dunne, A. & Monaghan, M. G. The Role of Macrophages in the Infarcted Myocardium: Orchestrators of ECM Remodeling. *Front. Cardiovasc. Med.* **6**, 101 (2019).

38. Fadok, V. A. *et al.* Macrophages that have ingested apoptotic cells in vitro inhibit proinflammatory cytokine production through autocrine/paracrine mechanisms involving TGF-beta, PGE2, and PAF. *J. Clin. Invest.* **101**, 890–898 (1998).

39. Yao, Y., Xu, X.-H. & Jin, L. Macrophage Polarization in Physiological and Pathological Pregnancy. *Front. Immunol.* **10**, 792 (2019).

40. Noy, R. & Pollard, J. W. Tumor-associated macrophages: from mechanisms to therapy. *Immunity* **41**, 49–61 (2014).

41. Yang, L. & Zhang, Y. Tumor-associated macrophages: from basic research to clinical application. *J. Hematol. Oncol.* **10**, 58 (2017).

42. Ferrante, C. J. *et al.* The adenosine-dependent angiogenic switch of macrophages to an M2-like phenotype is independent of interleukin-4 receptor alpha (IL-4Rα) signaling. *Inflammation* **36**, 921–931 (2013).

43. Wang, L., Zhang, S., Wu, H., Rong, X. & Guo, J. M2b macrophage polarization and its

roles in diseases. *J. Leukoc. Biol.* **106**, 345–358 (2019).

44. Hume, D. A. Macrophages as APC and the Dendritic Cell Myth. *J. Immunol.* **181**, 5829 LP – 5835 (2008).

45. Guilliams, M. *et al.* Dendritic cells, monocytes and macrophages: a unified nomenclature based on ontogeny. *Nat. Rev. Immunol.* **14**, 571–578 (2014).

46. DeNardo, D. G. & Ruffell, B. Macrophages as regulators of tumour immunity and immunotherapy. *Nat. Rev. Immunol.* **19**, 369–382 (2019).

47. Su, W. *et al.* The Polycomb Repressor Complex 1 Drives Double- Negative Prostate Cancer Metastasis by Coordinating Stemness and Immune Suppression Article The Polycomb Repressor Complex 1 Drives Double-Negative Prostate Cancer Metastasis by Coordinating Stemness and Imm. *Cancer Cell* **36**, 139-155.e10 (2019).

48. Mitri, D. Di *et al.* Re-education of Tumor-Associated Macrophages by CXCR2 Blockade Drives Senescence and Tumor Inhibition in Advanced Prostate Cancer Article Re-education of Tumor-Associated Macrophages by CXCR2 Blockade Drives Senescence and Tumor Inhibition in Advanced Pro. *CellReports* **28**, 2156-2168.e5 (2019).

49. Devalaraja, S. *et al.* Tumor-Derived Retinoic Acid Regulates Intratumoral Monocyte Differentiation to Promote Immune Suppression. *Cell* **180**, 1098-1114.e16 (2020).

50. Georgouli, M. *et al.* Regional Activation of Myosin II in Cancer Cells Drives Tumor Progression via a Secretory Cross-Talk with the Immune Microenvironment. *Cell* **176**, 757-774.e23 (2019).

51. Fisher, R., Pusztai, L. & Swanton, C. Cancer heterogeneity: implications for targeted therapeutics. *Br. J. Cancer* **108**, 479–485 (2013).

52. Meacham, C. E. & Morrison, S. J. Tumour heterogeneity and cancer cell plasticity. *Nature*

501, 328–337 (2013).

53. Dunn, G. P., Koebel, C. M. & Schreiber, R. D. Interferons, immunity and cancer immunoediting. *Nat. Rev. Immunol.* **6**, 836–848 (2006).

54. Ostrand-Rosenberg, S. Immune surveillance: a balance between protumor and antitumor immunity. *Curr. Opin. Genet. Dev.* **18**, 11–18 (2008).

55. Smyth, M. J., Dunn, G. P. & Schreiber, R. D. B. T.-A. in I. Cancer Immunosurveillance and Immunoediting: The Roles of Immunity in Suppressing Tumor Development and Shaping Tumor Immunogenicity. in *Cancer Immunotherapy* **90**, 1–50 (Academic Press, 2006).

56. Osipov, A., Murphy, A. & Zheng, L. Chapter Two - From immune checkpoints to vaccines: The past, present and future of cancer immunotherapy. in *Immunotherapy of Cancer* (eds. Wang, X.-Y. & Fisher, P. B. B. T.-A. in C. R.) **143**, 63–144 (Academic Press, 2019).

57. Chapman, J. R., Webster, A. C. & Wong, G. Cancer in the transplant recipient. *Cold Spring Harb. Perspect. Med.* **3**, a015677 (2013).

58. Matser, Y. A. H. *et al.* Transmission of breast cancer by a single multiorgan donor to 4 transplant recipients. *Am. J. Transplant.* **18**, 1810–1814 (2018).

59. Langley, R. R. & Fidler, I. J. The seed and soil hypothesis revisited--the role of tumor-stroma interactions in metastasis to different organs. *Int. J. cancer* **128**, 2527–2535 (2011).

60. Bos, P. D. *et al.* Genes that mediate breast cancer metastasis to the brain. *Nature* **459**, 1005–1009 (2009).

61. Kim, M.-Y. *et al.* Tumor Self-Seeding by Circulating Cancer Cells. *Cell* **139**, 1315–1326 (2009).

62. Aras, S. & Zaidi, M. R. TAMeless traitors: macrophages in cancer progression and metastasis. *Br. J. Cancer* **117**, 1583–1591 (2017).

63. Kaplan, R. N. *et al.* VEGFR1-positive haematopoietic bone marrow progenitors initiate the pre-metastatic niche. *Nature* **438**, 820–827 (2005).

64. Wculek, S. K. & Malanchi, I. Neutrophils support lung colonization of metastasis-initiating breast cancer cells. *Nature* **528**, 413–417 (2015).

65. Cools-Lartigue, J. *et al.* Neutrophil extracellular traps sequester circulating tumor cells and promote metastasis. *J. Clin. Invest.* **123**, 3446–3458 (2013).

66. Salgado, R. *et al.* The evaluation of tumor-infiltrating lymphocytes (TILs) in breast cancer: recommendations by an International TILs Working Group 2014. *Ann. Oncol.* **26**, 259–271 (2015).

67. Zitvogel, L. *et al.* The anticancer immune response: indispensable for therapeutic success? *J. Clin. Invest.* **118**, 1991–2001 (2008).

68. Pardoll, D. M. The blockade of immune checkpoints in cancer immunotherapy. *Nat. Rev. Cancer* **12**, 252–264 (2012).

69. Howlader N, Noone AM, Krapcho M, Miller D, Brest A, Yu M, Ruhl J, Tatalovich Z, Mariotto A, Lewis DR, Chen HS, Feuer EJ, C. K. (eds). SEER Cancer Statistics Review, 1975-2017. *National Cancer Institute* (2019). Available at: https://seer.cancer.gov/csr/1975_2017/.

70. Rawla, P., Sunkara, T. & Gaduputi, V. Epidemiology of Pancreatic Cancer: Global Trends, Etiology and Risk Factors. *World J. Oncol.* **10**, 10–27 (2019).

71. Yachida, S. *et al.* Distant metastasis occurs late during the genetic evolution of pancreatic cancer. *Nature* **467**, 1114–1117 (2010).

72. Thomas, D. & Radhakrishnan, P. Tumor-stromal crosstalk in pancreatic cancer and tissue fibrosis. *Mol. Cancer* **18**, 14 (2019).

73. Halbrook, C. J. *et al.* Macrophage-Released Pyrimidines Inhibit Gemcitabine Therapy in Pancreatic Cancer Short Article Macrophage-Released Pyrimidines Inhibit Gemcitabine Therapy in Pancreatic Cancer. *Cell Metab.* **29**, 1390-1399.e6 (2019).

74. Zhu, Y. *et al.* Tissue-Resident Macrophages in Pancreatic Ductal Adenocarcinoma Originate from Embryonic Hematopoiesis and Promote Tumor Progression. *Immunity* **47**, 323-338.e6 (2017).

75. Beatty, G. L. *et al.* Exclusion of T Cells From Pancreatic Carcinomas in Mice Is Regulated by Ly6C(low) F4/80(+) Extratumoral Macrophages. *Gastroenterology* **149**, 201–210 (2015).

76. Sanford, D. E. *et al.* Inflammatory monocyte mobilization decreases patient survival in pancreatic cancer: a role for targeting the CCL2/CCR2 axis. *Clin. Cancer Res.* **19**, 3404–3415 (2013).

77. Hingorani, S. R. *et al.* Trp53R172H and KrasG12D cooperate to promote chromosomal instability and widely metastatic pancreatic ductal adenocarcinoma in mice. *Cancer Cell* **7**, 469–483 (2005).

78. Zhang, X., Goncalves, R. & Mosser, D. M. The isolation and characterization of murine macrophages. *Curr. Protoc. Immunol.* **Chapter 14**, Unit-14.1 (2008).

79. Weisberg, S. P. *et al.* Tissue-Resident Memory T Cells Mediate Immune Homeostasis in the Human Pancreas through the PD-1/PD-L1 Pathway. *Cell Rep.* **29**, 3916-3932.e5 (2019).

80. Baklaushev, V. P. *et al.* Luciferase Expression Allows Bioluminescence Imaging But Imposes Limitations on the Orthotopic Mouse (4T1) Model of Breast Cancer. *Sci. Rep.* **7**, 7715 (2017).

81. Limberis, M. P., Bell, C. L. & Wilson, J. M. Identification of the murine firefly luciferase-

specific CD8 T-cell epitopes. *Gene Ther.* **16**, 441–447 (2009).

82. Kolaczkowska, E. & Kubes, P. Neutrophil recruitment and function in health and inflammation. *Nat. Rev. Immunol.* **13**, 159–175 (2013).

83. Yamada, K. M. & Sixt, M. Mechanisms of 3D cell migration. *Nat. Rev. Mol. Cell Biol.* **20**, 738–752 (2019).

84. Petrie, R. J., Doyle, A. D. & Yamada, K. M. Random versus directionally persistent cell migration. *Nat. Rev. Mol. Cell Biol.* **10**, 538–549 (2009).

85. Zengel, P. *et al.* μ-Slide Chemotaxis: A new chamber for long-term chemotaxis studies. *BMC Cell Biol.* **12**, 21 (2011).

86. Tranquillo, R. T., Lauffenburger, D. A. & Zigmond, S. H. A stochastic model for leukocyte random motility and chemotaxis based on receptor binding fluctuations. *J. Cell Biol.* **106**, 303–309 (1988).

87. Tharp, W. G. *et al.* Neutrophil chemorepulsion in defined interleukin-8 gradients in vitro and in vivo. *J. Leukoc. Biol.* **79**, 539–554 (2006).

88. Wu, P. H., Giri, A. & Wirtz, D. Statistical analysis of cell migration in 3D using the anisotropic persistent random walk model. *Nat. Protoc.* **10**, 517–527 (2015).

89. Wu, P.-H., Giri, A., Sun, S. X. & Wirtz, D. Three-dimensional cell migration does not follow a random walk. *Proc. Natl. Acad. Sci.* **111**, 3949 LP – 3954 (2014).

90. Jablonski, K. A. *et al.* Novel Markers to Delineate Murine M1 and M2 Macrophages. *PLoS One* **10**, e0145342–e0145342 (2015).

91. Phillip, J. M. *et al.* Fractional re-distribution among cell motility states during ageing. *bioRxiv* 2020.04.29.069286 (2020). doi:10.1101/2020.04.29.069286

92. Schrader, J. *et al.* Matrix stiffness modulates proliferation, chemotherapeutic response, and

dormancy in hepatocellular carcinoma cells. *Hepatology* **53**, 1192–1205 (2011).

93. McWhorter, F. Y., Wang, T., Nguyen, P., Chung, T. & Liu, W. F. Modulation of macrophage phenotype by cell shape. *Proc. Natl. Acad. Sci. U. S. A.* **110**, 17253–17258 (2013).

94. Rostam, H. M., Reynolds, P. M., Alexander, M. R., Gadegaard, N. & Ghaemmaghami, A. M. Image based Machine Learning for identification of macrophage subsets. *Sci. Rep.* **7**, 3521 (2017).

95. Genin, M., Clement, F., Fattaccioli, A., Raes, M. & Michiels, C. M1 and M2 macrophages derived from THP-1 cells differentially modulate the response of cancer cells to etoposide. *BMC Cancer* **15**, 577 (2015).

96. Park, E. K. *et al.* Optimized THP-1 differentiation is required for the detection of responses to weak stimuli. *Inflamm. Res.* **56**, 45–50 (2007).

97. Chanput, W., Peters, V. & Wichers, H. THP-1 and U937 Cells BT - The Impact of Food Bioactives on Health: in vitro and ex vivo models. in (eds. Verhoeckx, K. et al.) 147–159 (Springer International Publishing, 2015). doi:10.1007/978-3-319-16104-4_14

98. Wang, X. & Lin, Y. Tumor necrosis factor and cancer, buddies or foes? *Acta Pharmacol. Sin.* **29**, 1275–1288 (2008).

99. Schindelin, J. *et al.* Fiji: an open-source platform for biological-image analysis. *Nat. Methods* **9**, 676–682 (2012).

Supplemental Information 1

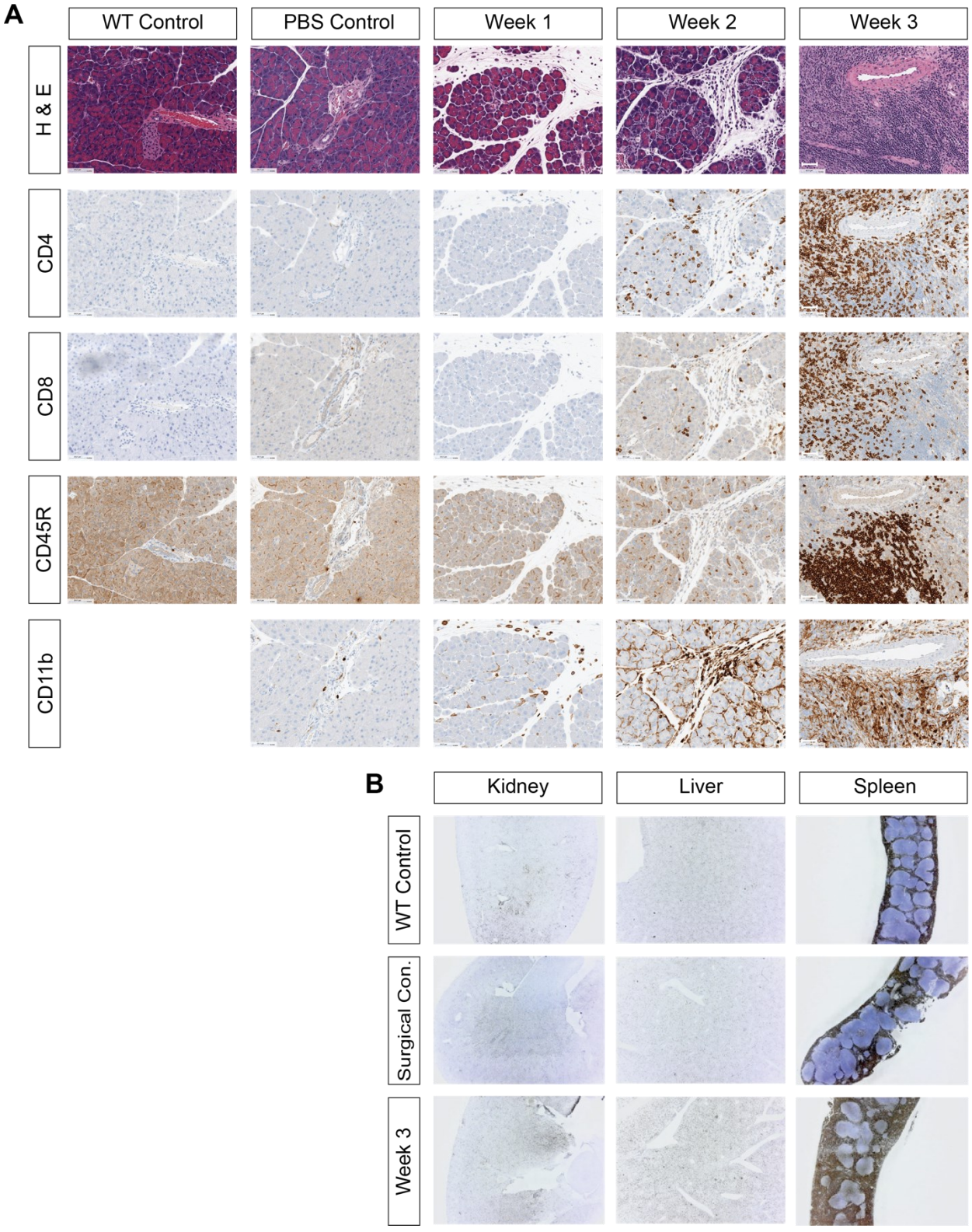

Figure S1. IHC Scans for Immune Landscape Characterizations

(A) Pathological slides of the pancreas. Same field of view was manually registered for each subject. $CD11b^+$ IHC staining for wild type control was damaged during processing. CD45R background signals may have interfered with the quantification of wildtype and PBS surgical controls. Overall CD45R signals are below 10%. Scale bar, 50 μm. n = 1 subject.

(B) $F4/80^+$ IHC staining for distinct organs. Enhanced F4/80 signals were observed for cancer cell implanted group at week 3 in comparison to both WT control and PBS surgical control group. n = 1 subject.

Supplemental Information 2

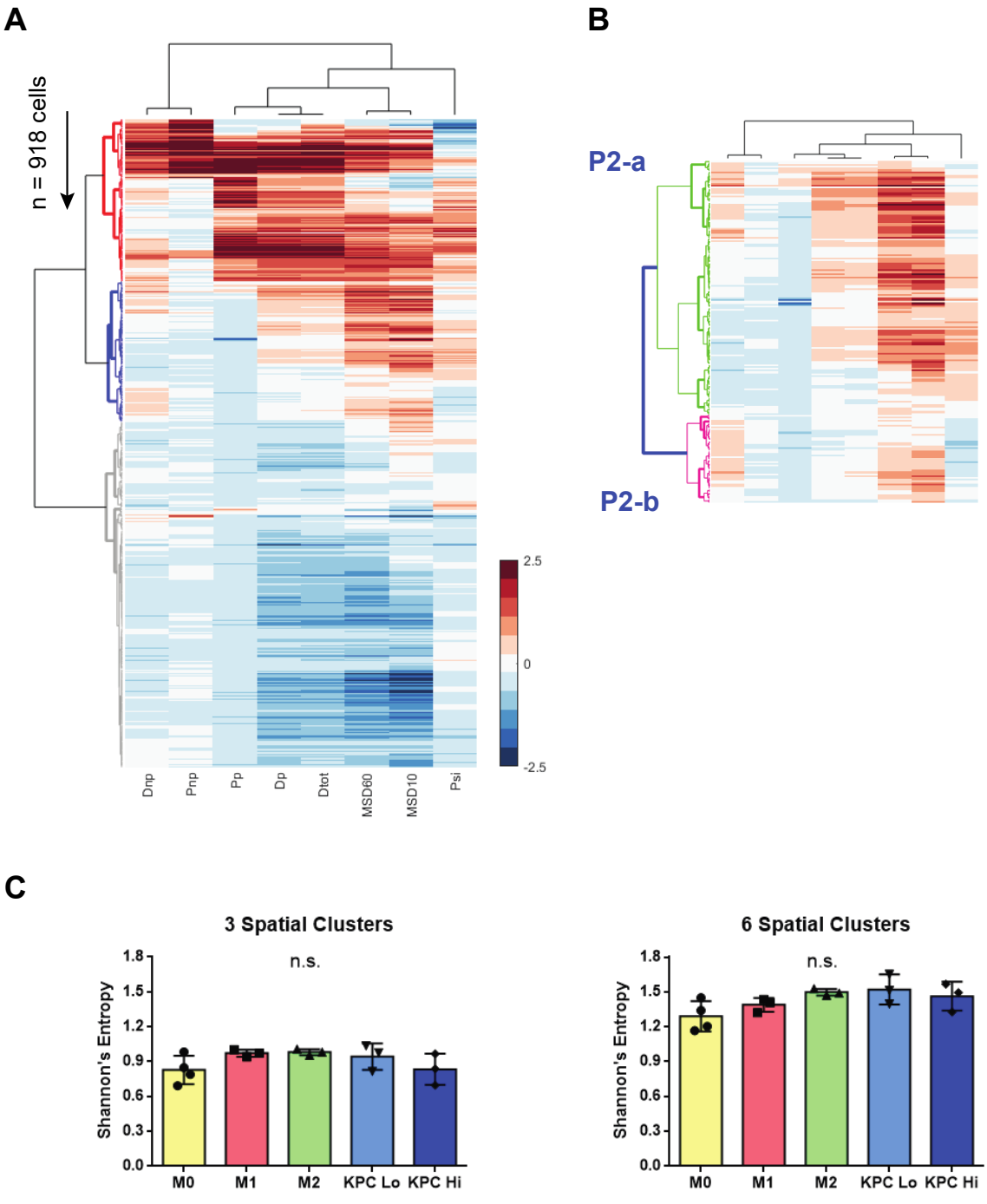

Figure S2. Clustering Rationales

(A) BMDM motility spatial clustering with 3 clusters as oppose to 8 clusters shown in Figure 9. Same 'cosine' distances and 'ward' linkages were used for computing dendrograms.

(B) Magnified view of cluster 2 from Figure S2A. This cluster has two distinct heatmap patterns P2-a and P2b, corresponding to the P3 and P4 from the 8 cluster dendrogram shown in Figure 9 respectively. The differential D_p, D_{tot}, Psi patterns between these two clusters suggests 3 cluster classification is underrepresenting the true heterogenicity of the population.

(C) Shannon's entropy calculated for 3 spatial cluster distribution and 6 spatial cluster distribution. Although the magnitude of spatial motility heterogenicity are higher in those with 6 cluster distribution, the overall trend between conditions are conserved.

Supplemental Information 3

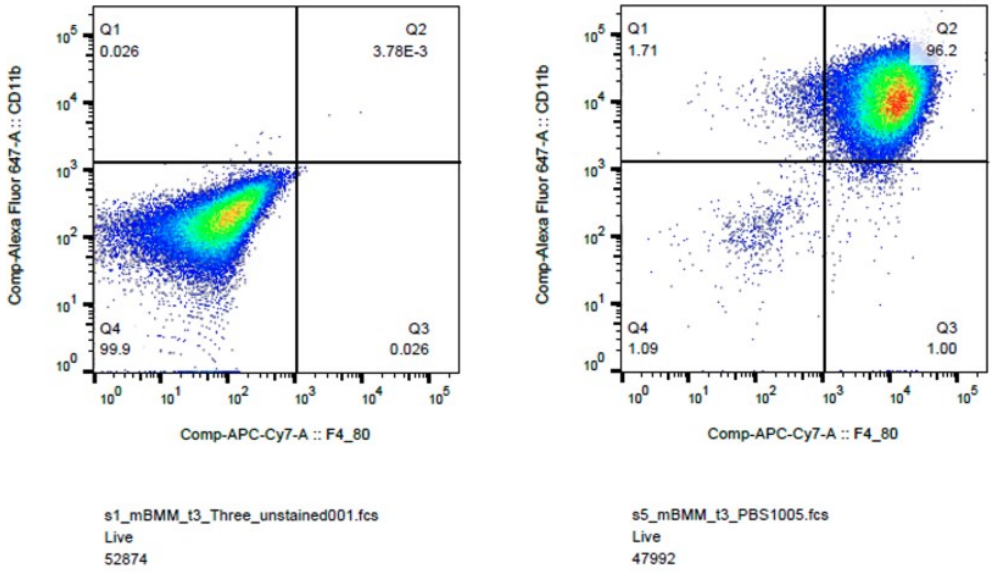

Figure S3. Flow Cytometry Confirm BMDM are CD11b$^+$ F4/80$^+$ Macrophage

Unstained (left) and PBS surgical control groups BMDM (right) are shown in pseudo-color bivariate density plot. CD11b signal is shown on the y-axis, and F4/80 signal is shown on the x-axis. The populations shown are live singlets gated based on forward and sideward scattering. The majority (>95%) of the bone marrow derived cells from surgical control group are CD11b$^+$ F4/80$^+$ macrophages.

Appendix A – List of Abbreviations

Abbreviation	Full Name/Definition	Abbreviation	Full Name/Definition
APRW	Anisotropic Persistent Random Walk	Itgam	Integrin Subunit Alpha M
B7-2	CD86 Molecule	KPC	Mouse PDAC model cells
BMDM	Bone Marrow Derived Macrophage	LDL	Low-density lipoproteins
C5aR1	Complement C5a Receptor 1	LPS	Lipopolysaccharide
CCR2	C-C Motif Chemokine Receptor 2	LTA	Lipoteichoic acid
CD	Cluster of Differentiation	M-CSF	Macrophage colony-stimulating factor
CD11b	Integrin Subunit Alpha M	M0	Naïve macrophage phenotype
CD14	Monocyte marker	M1	Pro-inflammatory macrophage phenotype
CD206	Mannose receptor	M2	Anti-inflammatory macrophage phenotype
CD38	ADP-Ribosyl Cyclase 1	MCP-1	CCL2, Monocyte chemoattractant protein-1
CD4	T helper maker	MGL-1	Macrophage galactose-type lectin-1
CD45R	B cell marker	MHC	Major Histocompatibility Complex
CD8	Cytotoxic T marker	MHC II	Major Histocompatibility Complex Class II
CD80	B7-1	MMP	Matrix metalloproteases
CD86	B7-2	MR	Mannose receptor
CpG-ODN	CpG oligodeoxynucleotides	MRC1	Mannose Receptor C-Type 1
CR3	Complement receptor 3	MSD	Mean-squared displacement
CSF1R	Colony Stimulating Factor 1 Receptor	NK	Natural killer cell
CXCR4	C-X-C Motif Chemokine Receptor 4	NO	Nitric Oxide
DAMP	Damage-associated molecular pattern	PAF	Platelet-activating factor
DC	Dendritic cell	PAMP	Pathogen-associated molecular pattern
DMEM	Dulbecco's Modified Eagle Medium	PBS	Phosphate-buffered saline
ECM	Extracellular matrix	PD-L1/2	Programmed death-ligand 1/2
EGF	Epidermal growth factor	PDAC	Pancreatic ductal adenocarcinoma
EGR2	Early Growth Response 2, transcription factor	PDGF-BB	Platelet-derived growth factor BB
F4/80	EGF-TM7 famioy, pan macropahge marker	PGE2	Prostaglandin E2
FACS	Fluorescence activated cell sorting	PGN	Peptidoglycan
FcγRI	Immunoglobulin Gamma Fc Receptor I	PI3kγ	Phosphoinositide 3-kinase γ
GPI	Glycosylphosphatidylinositol	PMA	Phorbol 12-myristate-13-acetate
H&E	Hematoxylin and eosin	PRW	Persistent Random Walk
HLA-DR	MHC Class II, DR	RPMI	Roswell Park Memorial Institute media
IFN-γ	Interferon gamma	RT-qPCR	Real Time quantitative PCR
IgG1	Immunoglobulin G1	SDF1α	Stromal cell-derived factor 1 alpha
IL-10	Interleukin 10	SIRPα	Signal regulatory protein α
IL-12	Interleukin 12	TGF-β	Transforming growth factor beta
IL-13	Interleukin 13	Tie2	Tyrosine-Protein Kinase Receptor TEK
IL-1ra	Interleukin-1 receptor antagonist	TLR	Toll-like receptor
IL-1β	Interleukin 1 beta	TME	Tumor microenvironment
IL-23	Interleukin 23	TNF-α	Tumor necrosis factor Alpha
IL-4	Interleukin 4	V(D)J	Variable (V), diversity (D) and joining (J) genes
IL-6	Interleukin 6	VEGF	Vascular endothelial growth factor
iNOS	Inducible nitric oxide synthase	WT	Wild type

Appendix B – Key Equations used for Calculations

Calculating 1-D displacement (x(t))

$$x(t) = \sqrt{\Delta x^2 + \Delta y^2}$$

$$\Delta x = x(t) - x(t-1);\ \Delta y = y(t) - y(t-1)$$

Z-score normalization (z)

μ is the mean, σ is the standard deviation

$$z = \frac{x - \mu}{\sigma}$$

Diffusivity along primary axis (D_p)

S_p is the speed along primary axis, P_p is the persistence time along primary axis

$$D_p = \frac{S_p^2 * P_p^2}{4}$$

Diffusivity along secondary axis (D_{np})

S_{np} is the speed along secondary axis, P_{np} is the persistence time along secondary axis

$$D_{np} = \frac{S_{np}^2 * P_{np}^2}{4}$$

Total diffusivity (D_{tot})

$$D_{tot} = D_p + D_{np}$$

Anisotropy (ψ)

$$\psi = \frac{D_p}{D_{np}}$$

Shannon's entropy (S)

p_i is the fractional abundance of cells in cluster i, N is the total number of clusters within a condition

$$S = -\sum_{i}^{N} p_i * \ln(p_i)$$

APRW Parameters

APRW parameters such as $S_p, S_{np}, P_p,$ and P_{np} were calculated by fitting the cell trajectory data based on published MATLAB scripts[88].

Appendix C – List of RT-qPCR Primers

Table 4. List of Human RT-qPCR Primers Used

Gene		Forward		Reverse
B-actin	5'-	CATGTACGTTGCTATCCAGGC	5'-	CTCCTTAATGTCACGCACGAT
ARG1	5'-	TGGACAGACTAGGAATTGGCA	5'-	CCAGTCCGTCAACATCAAAACT
CXCL10	5'-	GTGGCATTCAAGGAGTACCTC	5'-	TGATGGCCTTCGATTCTGGATT
CXCR2	5'-	CCTGTCTTACTTTTCCGAAGGAC	5'-	TTGCTGTATTGTTGCCCATGT
IL10	5'-	ACGGCGCTGTCATCGATTT	5'-	TGGAAGCTTCTGTTGGCTCC
IL12B	5'-	GCGGAGCTGCTACACTCTC	5'-	CCATGACCTCAATGGGCAGAC
IL1B	5'-	ATGATGGCTTATTACAGTGGCAA	5'-	GTCGGAGATTCGTAGCTGGA
IL6	5'-	ACTCACCTCTTCAGAACGAATTG	5'-	CCATCTTTGGAAGGTTCAGGTTG
MRC1	5'-	GGGTTGCTATCACTCTCTATGC	5'-	TTTCTTGTCTGTTGCCGTAGTT
Siglec10	5'-	TGGCTCAGAAGCGGAATC	5'-	CCTCATTGGAACTTGACTTCTGC
TBP	5'-	GAGCCAAGAGTGAAGAACAGTC	5'-	GCTCCCCACCATATTCTGAATCT
TNFa set 1	5'-	CCTCTCTCTAATCAGCCCTCTG	5'-	GAGGACCTGGGAGTAGATGAG
TNFa set 2	5'-	GAGGCCAAGCCCTGGTATG	5'-	CGGGCCGATTGATCTCAGC

Table 5. List of Mouse RT-qPCR Primers Used

Gene		Forward		Reverse
Arg1	5'-	CTCCAAGCCAAAGTCCTTAGAG	5'-	AGGAGCTGTCATTAGGGACATC
B-actin set 1	5'-	ATGAGCTGCCTGACGGCCAGGTCATC	5'-	TGGTACCACCAGACAGCACTGTGTTG
B-actin set 2	5'-	GGCTGTATTCCCCTCCATCG	5'-	CCAGTTGGTAACAATGCCATGT
CD206	5'-	CTCTGTTCAGCTATTGGACGC	5'-	CGGAATTTCTGGGATTCAGCTTC
CD38	5'-	TCTCTAGGAAAGCCCAGATCG	5'-	GTCCACACCAGGAGTGAGC
Cfd	5'-	CATGCTCGGCCCTACATGG	5'-	CACAGAGTCGTCATCCGTCAC
EGR2	5'-	GCCAAGGCCGTAGACAAAATC	5'-	CCACTCCGTTCATCTGGTCA
Fpr1	5'-	CCATTTGGTTGGTTCATGTGC	5'-	CTTCTTGGCTAGGCTCACAGT
Fpr2 set 1	5'-	GAGCCTGGCTAGGAAGGTG	5'-	TGCTGAAACCAATAAGGAACCTG
Fpr2 set 2	5'-	TCTACCATCTCCAGAGTTCTGTGG	5'-	TTACATCTACCACAA TGTGAACTA
Gpr18	5'-	CACCCTGAGCAATCACAACCA	5'-	AGTGACATTAACAAACAGCCCA
Hprt set 1	5'-	TGAAGAGCTACTGTAATGATCAGTCAAC	5'-	AGCAAGCTTGCAACCTTAACCA
Hprt set 2	5'-	TCAGTCAACGGGGGACATAAA	5'-	GGGGCTGTACTGCTTAACCAG
Ifit3	5'-	TCAGGCTTACGTTGACAAGGT	5'-	CACACTTTAGGCGTGTCCATC
IL6	5'-	CTGCAAGAGACTTCCATCCAG	5'-	AGTGGTATAGACAGGTCTGTTGG
iNOS	5'-	GTTCTCAGCCCAACAATACAAGA	5'-	GTGGACGGGTCGATGTCAC
Mgl2	5'-	TTAGCCAATGTGCTTAGCTGG	5'-	GGCCTCCAATTCTTGAAACCT
Ms4a4c	5'-	TGCAACTGCAAGCATAATGGG	5'-	GCAATGGTTGAAGCGTCACA
Ptgs1	5'-	ATGAGTCGAAGGAGTCTCTCG	5'-	GCACGGATAGTAACAACAGGGA
RPL13A	5'-	CGGACCGTGCGAGGTAT	5'-	CACCATCCGCTTTTTCTTGTC
S100a4	5'-	TGAGCAACTTGGACAGCAACA	5'-	CTTCTTCCGGGGCTCCTTATC
Slc7a2	5'-	GGCACCTTCGACGAACTTCTT	5'-	CCCAAGCAGACTCTTTTACTCCA
Slfn4	5'-	AATCCACAGACATCCATAGAGCC	5'-	TCCGTGTCCTGATCGACAGT

Academic Vita

EDUCATION

Johns Hopkins University (Baltimore, MD) *Anticipated: May 2020*

M.S. in Chemical and Biomolecular Engineering

Thesis Project: Polarization and Recruitment of Tumor Associated Macrophages
Supervised by Professor Denis Wirtz

The Pennsylvania State University (University Park, PA) *Aug 2014 – Aug 2018*

B.S. in Chemical Engineering**,** Honors in Biochemistry and Molecular Biology

Schreyer Honors College; Tau Beta Pi (Engineering Honor Society)
Thesis: *Characterization of PAD4 Inhibition and its Anti-Cancer Effects via mTOR Pathway*
Supervised by Dr. Yanming Wang

University College London (London, United Kingdom) *Dec 2017 – Jun 2018*

Semester Abroad Program*,* Division of Biosciences

AWARD

Whitfield Research Endowment | Dean's List | AIChE Freshman Recognition

EXPERIENCE

Graduate Researcher, Wirtz Lab, Institute for NanoBioTechnology, JHU *Sep 2018 – Present*

- Performed high-throughput screenings for cancer mediated human macrophage activation and polarization (qPCR, flow cytometry, and microscopy)
- Implemented migratory characterizations using 3D collagen gel and spheroid systems
- Conducted morphological and biomolecular phenotyping using primary Human PBMCs
- Administered in vivo study using orthotopic mouse model of pancreatic cancer
- Collaborated with both internal and external partners as a NIH U01 grant/project liaison
- Organized weekly immunology journal club within the department

Researcher, Wang Lab, Department of Biochemistry and Molecular Biology, PSU *Dec 2016 – Jul2018*

- Examined anti-cancer effects of PAD4 enzyme inhibitors using Western Blot and qPCR
- Created CRISPR/Cas9 constructs for generating knockout cell lines
- Conducted pancreatic cancer cell growth inhibition studies using MTT assays
- Assisted on *in-vivo* cancer metastasis studies using syngeneic mouse models

Research Assistant, Bracewell Lab, Department of Biochemical Engineering, UCL *Jan – Jun 2018*

- Assisted on cell free protein synthesis projects using *E. coli* platforms
- Evaluated codon usage variations among *E. coli* strains with respect to target proteins
- Supported robust DASbox and Ambr 250 reactor runs while complying with GLP standards

Upstream Intern, Vaccine Process Development and Commercialization, Merck & Co. *May – Aug 2017*

- Generated Design of Experiments to build continuous in-line metabolite analytical model using Raman spectroscopy probes
- Constructed a scale-down model for a yeast fermentation process using 3L bioreactors
- Authored experimental protocols, study design, and technical data packages
- Planned and executed experimental studies while coordinating 4 scientists in a GMP facility

Researcher, Curtis Lab, Department of Chemical Engineering, PSU *Nov 2014 – Dec 2016*

- Performed axenic extraction and symbiosis studies on more than 10 algal cell lines
- Accomplished genetic transformation of 2 microalgae strains using agrobacterium mediated transformation for a waste water treatment project
- Mentored 3 new researchers to the level of experimentally proficient and autonomous

Researcher, Curtis Lab, Department of Chemical Engineering, PSU *Nov 2014 – Dec 2016*

- Performed axenic extraction and symbiosis studies on more than 10 algal cell lines
- Accomplished genetic transformation of 2 microalgae strains using agrobacterium mediated transformation for a waste water treatment project
- Mentored 3 new researchers to the level of experimentally proficient and autonomous

LEADERSHIP

Teaching Assistant, Molecular Thermodynamics, Department of Chemistry, Penn State

Mentorship Chair, American Institute of Chemical Engineers, Penn State

International Student Orientation (ISO) Leader, University Office of Global Programs, PSU

Student Program Coordinator, University Office of Global Programs, Penn State

PRESENTATION

Xu H., Chu T., Huang Q., Walston J., Wirtz D., Wu P. "Characterization of the Motility and Morphology of Lymphocytes as Biomarker for Aging". *8th International Conference on Bioengineering and Nanotechnology*, May 30, 2019. Baltimore, MD.

Xu H., Willis N., Curtis W. "Monoculture Extraction and Permeability Constraints of Hydrocarbon Producing Colony Alga Botryococcus braunii". *2016 College of Engineering Research Initiative Poster Symposium*, Dec 2, 2016. State College, PA.

Cook L., Fuente P., **Xu H.**, Fodor, J., Milosavljevic B. "Photo-induced Solid State Proton Transfer from Pyranine to Hydroxyl Anion". *Department of Chemistry Poster Symposium*, Apr 27, 2016. State College, PA.

PUBLICATION

Luo, S.*, **Xu, H.***, Zuo, Y. et al. A Review of Functional Electrical Stimulation Treatment in Spinal Cord Injury. *NeuroMolecular Medicine* (2020)doi:10.1007/s12017-019-08589-9
**Authors contributed equally*

SKILL

Laboratory

High-throughput Screening, Microscopy, Flow Cytometry, qPCR, Western Blot, Cloning, Mammalian Cell Culture, 3D Culture Systems, Bioreactor/Centrifuge Scaling

Computer

Python, MATLAB, SnapGene, Benchling, ELN, Microsoft Office, Aspen HYSYS

Language

Mandarin Chinese (native fluency)

REFERENCE

Available Upon Request